Summer 8-2014

Evaluation of the Performance of Various Turbulence Models for Accurate Numerical Simulation of a 2D Slot Nozzle Ejector

Colin Graham
Washington University in St Louis

WASHINGTON UNIVERSITY IN ST. LOUIS

School of Engineering and Applied Science

Department of Mechanical Engineering and Materials Science

Thesis Examination Committee:
Dr. Ramesh K. Agarwal (Chair)
Dr. David A. Peters
Dr. Frederick Roos

Evaluation of the Performance of Various Turbulence Models for Accurate Numerical Simulation of a 2D Slot Nozzle Ejector

by

Colin T. Graham

A thesis presented to the School of Engineering and Applied Science
of Washington University in St. Louis in partial fulfillment of the
requirements for the degree of
Master of Science

August 2014

Saint Louis, Missouri

Table of Contents

List of Figures

List of Tables

List of Symbols

ε	Turbulent Dissipation Rate
γ	Intermittency
k	Turbulent Kinetic Energy
μ	Turbulent Eddy Viscosity
σ	Turbulent Prandtl Number
Q_{SAS}	SAS-SST *k-ω* Turbulence Model Source Term
ρ	Density
S	Strain Rate
τ	Reynolds Shear Stress
t	Time
u	Velocity
ω	Psuedo-Vorticity
ν	Kinematic Eddy Viscosity

Acknowledgments

I would like to acknowledge Dr. Ramesh Agarwal for encouraging me to engage in graduate research and guiding me through this process. His knowledge of engineering fundamentals and computational fluid dynamics, as well as the ability to explain these concepts clearly, have helped me in completing this research with a greater understanding. I would like to acknowledge the doctoral candidate Tim Wray for helping me with the day to day issues of conducting CFD research.

I would like to thank my family and close friends for their continued support both emotionally and many times financially while I undertook this endeavor.

I would like to dedicate this thesis to my parents who always supported and encouraged me to explore my interests and my pursuit of knowledge.

Colin Graham

Washington University in St. Louis
August 2014

ABSTRACT

Evaluation of the Performance of Various Turbulence Models for Accurate Numerical Simulation of a 2D Slot Nozzle Ejector

by

Colin T. Graham

Master of Science in Mechanical Engineering

Washington University in St. Louis

Research Advisor: Dr. Ramesh Agarwal

With the development over the last several decades, accurate Computational Fluid Dynamics (CFD) modeling has now become an essential part in the analysis and design of various industrial products where the fluid flow plays an important role. The goal of this thesis is to apply the CFD technology to the analysis of a 2D slot nozzle ejector which has application in Short Take-off and Landing (STOL) aircraft and other future aerospace vehicles. In the nozzle-ejector configuration, the high speed air flow from the nozzle entrains the ambient air into a mixing chamber (ejector) as a means to create additional thrust for a STOL aircraft. In 1973, the effectiveness of a slot nozzle ejector configuration in generating additional thrust was evaluated experimentally by Gilbert and Hill of Dynatech under a NASA contract [1]. In this research, numerical simulations of this experimental configuration are performed and compared with the experimental data. An accurate computational model for simulations requires solving the appropriate governing equations of fluid dynamics using an accurate numerical algorithm on an appropriately clustered mesh in the computational domain [2]. We employ the Unsteady Reynolds-Averaged Navier-Stokes (URANS) equations to model the turbulent supersonic flow in the 2D slot nozzle ejector. These equations require the computation of

turbulent stresses which are modeled by using a turbulence model. The choice of a turbulence model can affect the accuracy of the solution because of their empirical nature. The goal of this research is to evaluate five turbulence models and determine the best possible model that can most accurately simulate the ejector nozzle mixing flow. The five turbulence models employed are the one-equation Spalart-Allmaras (SA) model, two-equation standard k-ε and SST k-ω models, the four-equation Transition SST model, and the SAS-SST k-ω model. The effectiveness of each turbulence model is determined by comparing the computational results with the experimental data. For the computations, an unstructured mesh is generated using the ICEM CFD 14.5 software and the flow field is calculated using the commercial CFD solver ANSYS-Fluent.

1 Introduction

This chapter introduces the motivation for Computational Fluid Dynamics (CFD) modeling of air to air ejectors, the background of the experiment to be simulated, and the goals of this research.

1.1 Motivation

Accurate numerical simulation of high speed ejector flow is critical for faster design and optimization of nozzle ejector systems. CFD modeling of the turbulent mixing between the high speed jet and the flow requires an accurate turbulence model when solving the Unsteady Reynolds-Averaged Navier-Stokes (URANS) equations. This research evaluates five turbulence models to determine the best model that gives the most accurate results for a slot nozzle ejector when compared to the experimental data of Gilbert and Hill [1].

1.2 Background

Since the mid-sixties, high speed ejector nozzles have been considered by NASA for use in Short Takeoff or Landing (STOL) aircraft as a wing lift augmenter. To aid in the development of these lift augmenters, a finite difference computer program was developed by NASA. In 1973, Gerald B. Gilbert and Philip G. Hill of Dynatech R/D Company were given the task of conducting an experiment to validate the finite difference computer program to calculate the flow in air to air ejectors [1]. Gilbert and Hill constructed an experimental apparatus to produce the two-dimensional ejector test data for comparison with the computational results. Figure 1.1 shows the experimental test setup involving a primary converging slot nozzle ejector with the discharge entering a symmetric variable area mixing section.

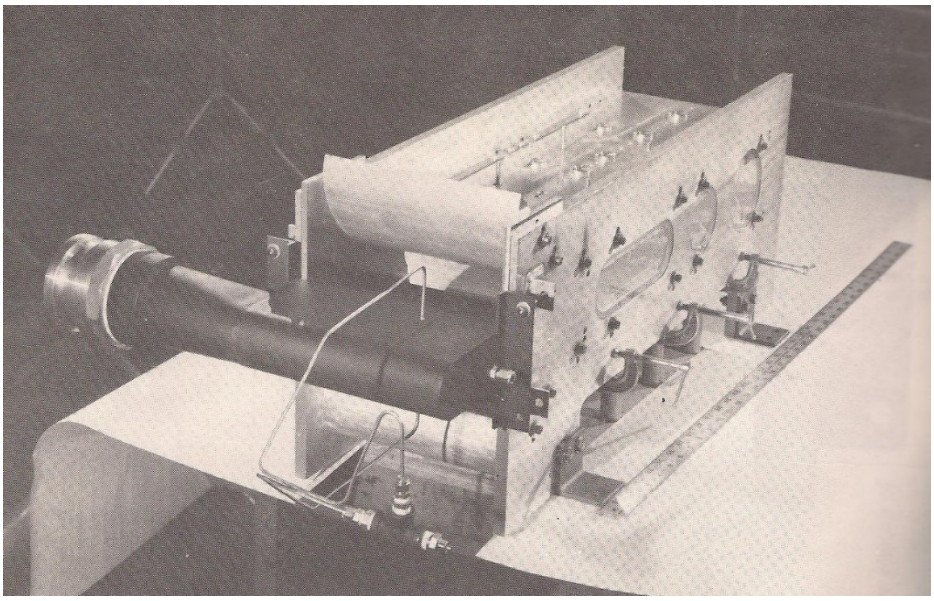

Figure 1.1 Slot Nozzle Ejector and Mixing Section [1].

The nozzle outlet geometry is of 0.1215" x 8" exit cross-section. The mixing section has two configurations with throat cross-sections of 1.25" x 8" and 1.875" x 8". Pressure and temperature measurements were taken at the mixing section wall at multiple distances from the nozzle discharge as shown in Figure 1.2.

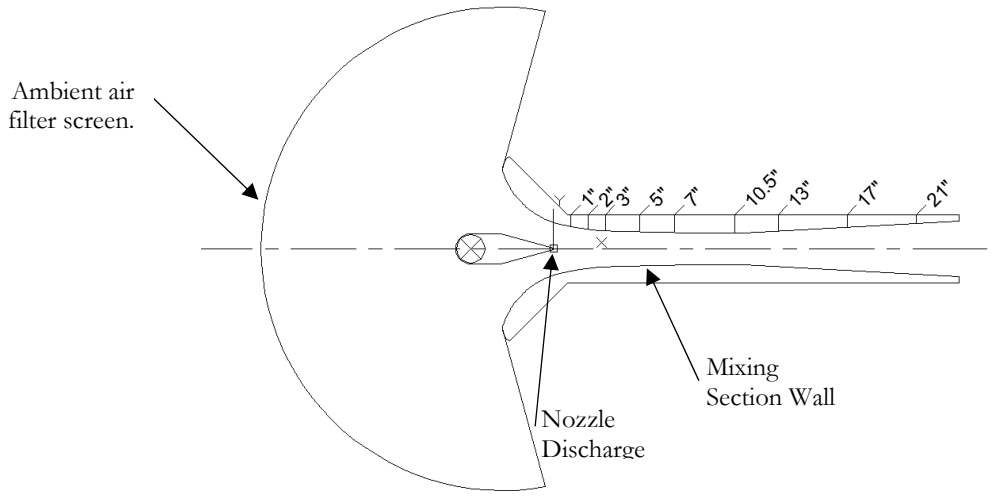

Figure 1.2 Experimental Cross Section and Measurement Locations.

Four operating flow rates were tested for both the mixing section throat heights by adding a series of restrictors to the mixing section outlet. The four cases included (a) the mixing section discharging

directly to the lab, (b) a plenum connected to the discharge, (c) an eight inch orifice connected to the plenum, and (d) a partially closed throttle valve added after the orifice to achieve the lowest flow rate. A schematic of the experimental apparatus is shown in Figure 1.3.

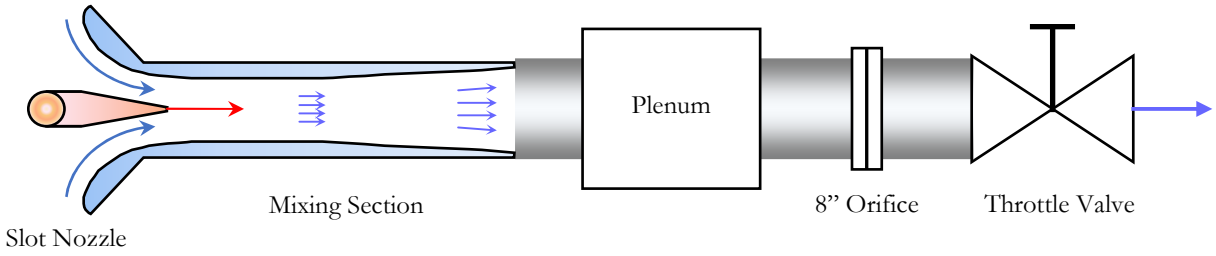

Figure 1.3 Schematic of Experiment Test Sections.

The high speed ejector flow pumps the ambient air through the mixing section. This increases the mass flow rate out of the mixing section as well as the thrust produced by the system. The air leaving the nozzle has a low mass flow rate but because of its high speed it has a lot of momentum. This momentum is transferred to the entrained ambient air in the ejector mixing section and thus the combined mass flow leaves the mixing section with higher momentum. As the high speed nozzle flow mixes with the low speed ambient entrained flow and moves towards the outlet, a region of low pressure is created in the mixing section. This pressure gradient further entrains the flow of ambient air into the mixing section and increases the mass flow rate out of the system. The existence of supersonic flow from the nozzle mixing with the entrained subsonic flow results in a turbulent mixing layer that adds to the complexity of modeling this flow field.

1.3 Goals and Objectives

The goal of the research is to apply the current CFD technology to the experimental configuration of Gilbert and Hill [1] and determine in particular which turbulence model (out of a suite of five models) produces the best results that most accurately reproduce the experimental data. The numerical model requires a quality mesh, accurate boundary conditions and an accurate solver to solve the governing equations of turbulent fluid flow.

2 Computational Methodology

This chapter describes the procedure for numerical simulation of the flow field inside the 2D slot nozzle ejector configuration.

2.1 Mesh Generation

The mesh inside the computational domain was generated by employing the commercial software ICEM CFD. The mesh was then imported into ANSYS Fluent software which was used for the numerical simulations of the flow field and adaptive refinement. The mesh was adapted based on gradients of the flow field variables. The solutions obtained with a coarse mesh and a very dense mesh were compared to determine a suitable mesh so that the computations were mesh independent.

2.1.1 ICEM CFD

A table of mixing section dimensions published by Gilbert and Hill [1] was used to create a point data file of the mixing section geometry which was then imported into ICEM CFD. The points were connected to create the walls of the mixing section and the primary nozzle was constructed within the mixing section inlet based on the experimental geometry. Because the nozzle and mixing section were symmetric about the longitudinal axis, only one half of the 2D cross-section was constructed. A mesh was then created (similar to that in the paper of Georgiadis and Yoder [3]) and refined so that the grid downstream of the nozzle discharge had 350 x 150 nodes. The mesh density was increased near the walls of the nozzle and the mixing section as well as in the assumed downstream path of the nozzle jet flow which included the mixing layer. Thus a 2D mesh with 63,000 nodes was generated. The quality of the mesh was checked to ensure that the Jacobian of all the node elements was at least above 0.7. On a scale from 0 to 1, the Jacobian of a node element would be 1 if it is a perfectly square element. Finally the mesh was checked for orthogonality and skewness near the boundaries of the computational domain. In ICEM CFD, the bounding surfaces can be set as boundary conditions for the flow field to export to Fluent.

2.1.2 Adaptive Meshing using Fluent

Once the flow solver Fluent gives a converged solution on an initial mesh, it has the ability to rearrange the density of the mesh based on gradients of the flow variables [4]. This feature is used to increase the mesh density in areas of large velocity, pressure, and density gradients to improve the accuracy of the solution. The adaptive meshing process begins with the selection of a proper flow variable (static pressure) needed for adaptation. Then the gradients of the flow variables are calculated and cells with highest gradients are determined. A minimum value of the gradient is specified for refining the mesh; Fluent then increases the density of the cells such that the gradient values in these cells are equal to or less than the specified value. Thus the increase in mesh density in a flow region is related to the magnitude of the flow gradients in that region. Since near the nozzle discharge area, there are multiple intersecting shockwaves where the gradients of fluid static pressure are very high, the mesh density is high. The initial grid is shown in Figure 2.1 and the result of the pressure gradient adaption of the grid is shown in Figure 2.2.

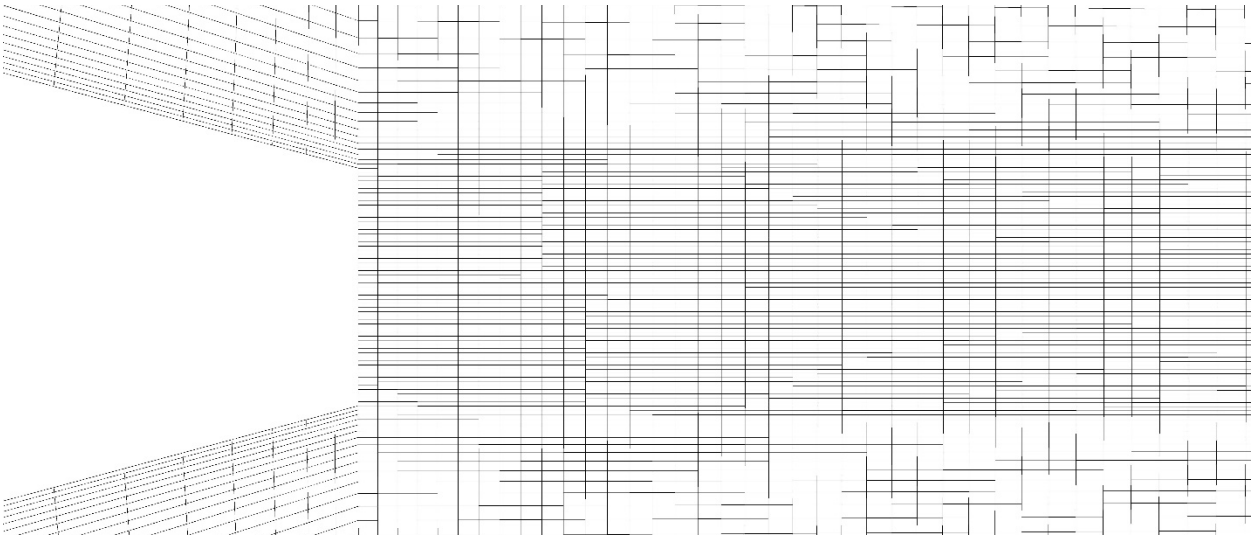

Figure 2.1 Mesh Density Downstream of the Nozzle Discharge prior to Adaption.

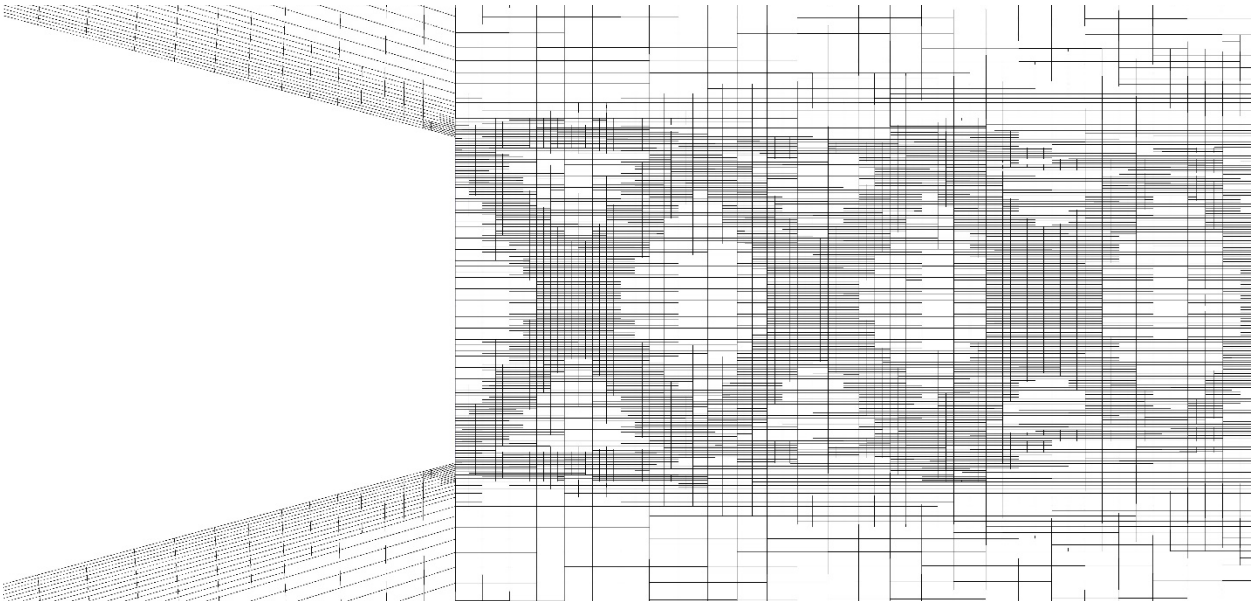

Figure 2.2 Mesh Density Downstream of the Nozzle Discharge after Adaption.

2.1.3 Comparison of Solution with Different Mesh Densities

The increase in mesh density usually leads to more accurate results but also increases the computational time. However, beyond a certain mesh density there is no appreciable change in the solution. A mesh comparison was conducted to determine an appropriate mesh density that would produce accurate results. A coarse mesh with nearly 63,000 cells and a dense mesh with nearly 200,000 cells were used in the simulations. Simulations were also performed on a coarse adapted mesh based on gradients of pressure, velocity, and density with nearly 90,000 cells. The results for the velocity profile at 4 inches downstream of the nozzle discharge using different mesh densities are compared with the experimental data in Figure 2.3.

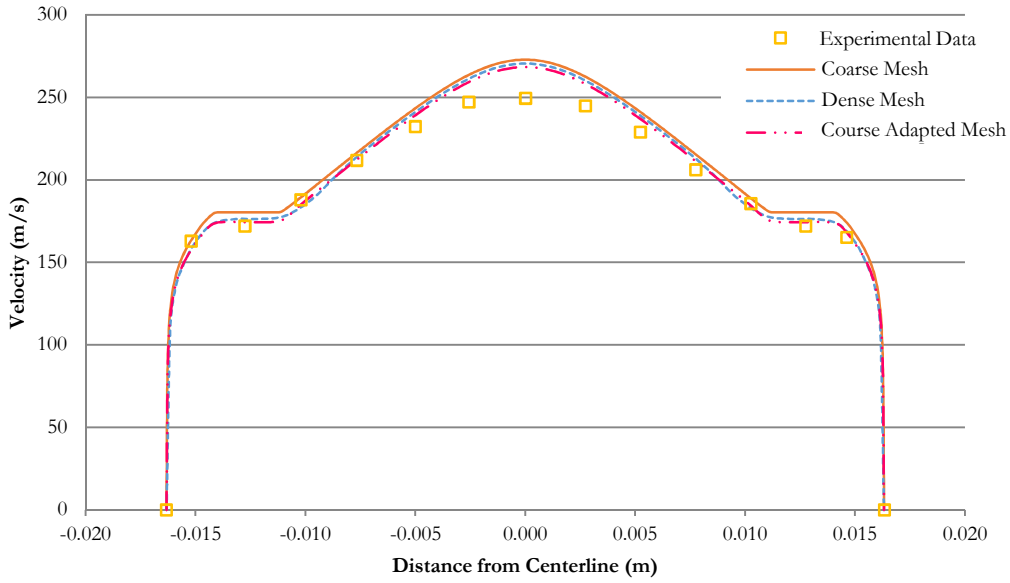

Figure 2.3 Comparison of Computed Velocity Profiles at a Distance of 7 inches from Nozzle Exit for Run #1 Obtained with Different Mesh Densities with the Experimental Data.

It can be seen from Figure 2.3 that the coarse mesh with mesh adaption gives results close to that obtained by the dense mesh. Therefore, all the simulations were performed using a gradient adapted mesh with 90,000 cells.

2.2 Numerical Solver

ANSYS Fluent was used to simulate the ejector nozzle flow field. The mesh is imported from ICEM CFD into Fluent. In Fluent, a steady-state density based finite-volume solver is employed for solution of URANS equations with five different turbulence models. Boundary and initial conditions are input into the solver. The numerical algorithm is second-order accurate.

2.2.1 Details of Simulation Methodology

In ANSYS Fluent, the mesh file from ICEM-CFD is imported and scaled to the dimensions in inches. To calculate the supersonic compressible flow, the flow solver option employed is density based. Furthermore, steady state algorithm is used since the test data was taken when the experiment was running at constant operating conditions. Only one simulation was run as transient with the SAS-SST k-ω turbulence model to capture the time dependent large scale turbulence effects. To

calculate the flow field, Unsteady Reynolds-Averaged Navier-Stokes (URANS) equations are employed in conjunction with a turbulence model. Fluent solves these equations at each node of the mesh [4]. Compressible URANS equations use mass-averaged values to define instantaneous flow variables when calculating the mean flow; it is also called the "Favre averaging." For example, in the Reynolds averaging the velocity is decomposed as:

$$u_i = \tilde{u}_i + u_i'' \tag{2.1}$$

where $\tilde{u}_i$ is the mean velocity and u_i'' is the fluctuating component of velocity. The mean velocity is averaged over a time period T as follows:

$$\tilde{u}_i = \frac{1}{T}\int_T u_i(t)dt\,. \tag{2.2}$$

Farve-averaging is density weighted averaging defined as:

$$\tilde{u}_i = \frac{\overline{\rho u_i}}{\bar{\rho}}. \tag{2.3}$$

Using Farve-averaging, the Navier-Stokes equations become:

$$\frac{\partial(\bar{\rho}\tilde{u}_i)}{\partial t} + \frac{\partial}{\partial x_j}\left(\bar{\rho}\tilde{u}_j\tilde{u}_i\right) = -\frac{\partial \bar{p}}{\partial x_i} + \frac{\partial}{\partial x_j}\left[\bar{t}_{ji} - \overline{\rho u_i'' u_i''}\right]. \tag{2.4}$$

As a result of averaging, an additional term called the Reynolds stress tensor appears in equation 2.4 which can be written as:

$$-\overline{\rho u_i'' u_j''} = \bar{\rho}\tau_{ij}. \tag{2.5}$$

Reynolds stress tensor given by equation 2.5 represents the rate of momentum transfer due to the turbulent velocity fluctuations [2]. In order to solve for the mean flow variables the Reynolds stress tensor needs to be mathematically modeled in order to address the so called 'closure problem.' Determining a suitable description of the Reynolds stress tensor to address the 'closure problem' is the purpose of turbulence modeling. In most of the turbulence models, the Reynolds stress tensor is defined by the Boussinesq approximation which assumes that the principal axes of the stress align with those of the mean strain-rate [2]. Then the Reynolds Stress tensor is defined by introducing the concept of turbulent eddy viscosity as follows:

$$\bar{\rho}\tau_{ij} = -\rho\overline{u_i' u_j'} = 2\mu_t \bar{S}_{ij} - \frac{2}{3}\bar{\rho}k\delta_{ij} \tag{2.6}$$

where μ_t denotes the eddy viscosity. The turbulent eddy viscosity, μ_t, is determined in terms of mean flow variables by a turbulence model [2]. There are a wide variety of turbulence models that have developed over the past ten decades. The selection of an appropriate turbulence model is

crucial for accurate CFD simulations using RANS equations, especially for complex flows. In this thesis, we choose five different turbulence models to evaluate their relative accuracy for computing the slot nozzle-ejector flow field.

2.2.2 Turbulence Models

The goal of this research is to determine which turbulence model (out of a suite of models) will most accurately reproduce the experimental results for the slot nozzle ejector using CFD. The turbulence models considered in this research are the SA, *k-ε*, SST *k-ω*, Transition SST, and SAS-SST *k-ω* models. The SA turbulence model is a one-equation transport model that solves for the kinematic eddy viscosity, $\tilde{v}$. It was designed for accurate modeling of aerodynamic flows and to be computationally efficient [5]. The transport equation for $\tilde{v}$ in the SA model can be expressed as:

$$\frac{\partial}{\partial t}(\rho\tilde{v}) + \frac{\partial}{\partial x_i}(\rho\tilde{v}u_i) = \frac{1}{\sigma_v}\left[\frac{\partial}{\partial x_j}\left\{(\mu + \rho\tilde{v})\frac{\partial\tilde{v}}{\partial x_j}\right\} + c_{b2}\rho\left(\frac{\partial\tilde{v}}{\partial x_j}\right)^2\right] + G_v - Y_v + S_{\tilde{v}}\,. \tag{2.7}$$

Expressions for several quantities and coefficients on RHS of equation 2.7 can be found in Ref. [5] and the ANSYS FLUENT Theory Guide. *k-ε* turbulence model is a two-transport-equation model solving for the kinetic energy *k* and the turbulent dissipation *ε*. The assumption in the derivation of the model that the effects of molecular viscosity are negligible limits it to be accurate only for fully turbulent flows [4]. It has also been found that the k-ε model is not very accurate in the presence of large pressure gradients [6]. In what follows, it should be noted that the bars are not included on the variables although they are Reynolds-averaged quantities. The transport equations for *k- ε* are given by:

$$\frac{\partial}{\partial t}(\rho k) + \frac{\partial}{\partial x_i}(\rho k u_i) = \frac{\partial}{\partial x_j}\left[\left(\mu + \frac{\mu_t}{\sigma_k}\right)\frac{\partial k}{\partial x_j}\right] + G_k + G_b - \rho\varepsilon - Y_M + S_k \tag{2.8}$$

$$\frac{\partial}{\partial t}(\rho\varepsilon) + \frac{\partial}{\partial x_i}(\rho\varepsilon u_i) = \frac{\partial}{\partial x_j}\left[\left(\mu + \frac{\mu_t}{\sigma_\varepsilon}\right)\frac{\partial\varepsilon}{\partial x_j}\right] + C_{1\varepsilon}\frac{\varepsilon}{k}(G_k + C_{3\varepsilon}G_b) - C_{2\varepsilon}\rho\frac{\varepsilon^2}{k} + S_\varepsilon\,. \tag{2.9}$$

Turbulent eddy viscosity, μ_t, is then determined using the equation:

$$\mu_t = \rho C_\mu \frac{k^2}{\varepsilon}. \tag{2.10}$$

k-ω turbulence model is also a two-transport-equation model solving for the kinetic energy *k* and turbulent pseudo-vorticity *ω*. The Shear Stress Transport (SST) version of the *k-ω* model combines the best features of the standard *k-ω* model near the wall and *k-ε* model in the free stream region to make use of their accuracy near walls and in the free stream respectively [4]. The transport equations of the SST *k-ω* model are as follows:

$$\frac{\partial}{\partial t}(\rho k) + \frac{\partial}{\partial x_i}(\rho k u_i) = \frac{\partial}{\partial x_j}\left[\left(\mu + \frac{\mu_t}{\sigma_k}\right)\frac{\partial k}{\partial x_j}\right] + \tilde{G}_k - Y_k + S_k \tag{2.11}$$

$$\frac{\partial}{\partial t}(\rho \omega) + \frac{\partial}{\partial x_i}(\rho \omega u_i) = \frac{\partial}{\partial x_j}\left[\left(\mu + \frac{\mu_t}{\sigma_\omega}\right)\frac{\partial \omega}{\partial x_j}\right] + \tilde{G}_\omega - Y_\omega + D_\omega + S_\omega\,. \tag{2.12}$$

For SST *k-ω* model μ_t is determined by the equation:

$$\mu_t = \rho \frac{k}{\varepsilon} \frac{1}{\max\left[\frac{1}{\alpha^*}, \frac{SF_2}{\alpha_1 \omega}\right]}. \tag{2.13}$$

Building upon the *k-ω* SST model is the Transition SST turbulence model which includes an equation for defining the transition from laminar to turbulent flow. The *ω* transport equation remains unchanged while the *k* transport equation is modified to include intermittency γ by including constants (γ, γ_{eff}, γ_{sep}) as given in equations 2.14 and 2.15 below. The modified *k* transport equation can be expressed as:

$$\begin{aligned} \frac{\partial}{\partial t}(\rho k) + \frac{\partial}{\partial x_i}(\rho k u_i) &= \frac{\partial}{\partial x_j}\left[\left(\mu + \frac{\mu_t}{\sigma_k}\right)\frac{\partial k}{\partial x_j}\right] \\ +\gamma_{eff}\tilde{G}_k - \min\left(max\left(\gamma_{eff}, 0.1\right), 1.0\right) Y_k + S_k \end{aligned} \tag{2.14}$$

where

$$\begin{aligned} \gamma_{eff} &= \max\left(\gamma, \gamma_{sep}\right) \\ \gamma_{sep} &= \min\left(C_{s1}\, max\left[\left(\frac{Re_v}{3.235 Re_{\theta c}}\right) - 1{,}0\right] F_{reattch}, 2\right) F_{\theta t}\,. \end{aligned} \tag{2.15}$$

The transport equation for intermittency γ is given by:

$$\frac{\partial}{\partial t}(\rho\gamma) + \frac{\partial}{\partial x_j}(\rho U_j) = \frac{\partial}{\partial x_j}\left[\left(\mu + \frac{\mu_t}{\sigma_\gamma}\right)\frac{\partial \gamma}{\partial x_j}\right] + P_{\gamma 1} - E_{\gamma 1} + P_{\gamma 2} - E_{\gamma 2}. \tag{2.16}$$

Another turbulence model in ANSYS Fluent is the Scale Adaptive Simulation (SAS) SST *k-ω* model which accounts for the large scales of turbulence and not just the dissipative scales [4]. The SAS-SST *k-ω* model employs an exact transport equation for turbulent kinetic energy times the length scale, *kL*. The transport equations for this model are given as:

$$\frac{\partial}{\partial t}(\rho k) + \frac{\partial}{\partial x_i}(\rho u_i k) = \frac{\partial}{\partial x_j}\left[\left(\mu + \frac{\mu_t}{\sigma_k}\right)\frac{\partial k}{\partial x_j}\right] + G_k - \rho c_\mu k\omega$$

$$\frac{\partial}{\partial t}(\rho\omega) + \frac{\partial}{\partial x_i}(\rho u_i \omega) = \alpha\frac{\omega}{k}G_k - \rho\beta\omega^2 + Q_{SAS} + \frac{\partial}{\partial x_j}\left[\left(\mu + \frac{\mu_t}{\sigma_\omega}\right)\frac{\partial \omega}{\partial x_j}\right] \tag{2.17}$$

$$+(1-F_1)\frac{2\rho}{\sigma_{\omega,2}}\frac{1}{\omega}\frac{\partial k}{\partial x_j}\frac{\partial \omega}{\partial x_j}$$

where the SAS source term is defined by:

$$Q_{SAS} = \max\left[\rho\eta_2 k S^2\left(\frac{L}{L_{vk}}\right)^2 - C\frac{2\rho k}{\sigma_\Phi} max\left(\frac{1}{\omega^2}\frac{\partial \omega}{\partial x_j}\frac{\partial \omega}{\partial x_j}, \frac{1}{k^2}\frac{\partial k}{\partial x_j}\frac{\partial k}{\partial x_j}\right), 0\right]. \tag{2.18}$$

In the 2D slot nozzle configuration, there is a mixture of flow types in the experiment involving compressible subsonic and supersonic flow regions including shock, the free-stream turbulence and the near-wall boundary layer flows. In this thesis, the results of the CFD analysis are compared to the experimental results to determine which turbulence model gives the best accuracy in modeling this complex flow field.

2.2.3 Initial and Boundary Conditions

Eight of the eleven experimental cases performed by Gilbert and Hill have data published in their report and therefore constitute the eight cases simulated in this thesis. In the experiment, runs #4, #8, and #11 were repetitions of previous runs and therefore no experimental data was recorded. Four runs using the 1.25 inch mixing section throat, and four runs using the 1.875 inch mixing section throat are simulated. Table 2.1 shows the operating conditions and boundary conditions used in simulation of each run. For each simulation the absolute pressure of air in the laboratory test was set. Then the gauge pressure at the mixing section inlet and at the outlet were set to 0 psi and

the temperature conditions were set to atmospheric. The nozzle discharge boundary gauge pressure and temperature were input from the experiment and the walls are treated as no-slip. The bottom of the computational domain was set as the symmetry boundary condition. The air is treated as an ideal gas. The material of the walls are aluminum.

Table 2.1 Geometry and the Flow Variables for Various Runs.

Run #	Nozzle Pressure psia	Nozzle Temp., °R	Nozzle Throat Area, in^2	Barometric Pressure psia	Atmospheric Temp., °R	Mixing Section Throat Size
1	31.69	641	0.9688	14.69	538	1.25"
2	31.60	637	0.9688	14.60	543	1.25"
3	31.61	706	0.9688	14.61	553	1.25"
5	31.71	648	0.9688	14.71	544	1.25"
6	35.80	649	0.9688	14.80	547	1.875"
7	35.80	647	0.9688	14.80	543	1.875"
9	35.73	644	0.9688	14.73	550	1.875"
10	35.70	660	0.9688	14.70	547	1.875"

The simulations using a pressure boundary condition at the nozzle inlet resulted in higher mass flow rates than what was determined experimentally; therefore four of the runs were simulated again using a mass flow rate boundary condition. First, the nozzle inlet boundary condition was set to the mass flow rate in Table 2.1 with mixing section outlet remaining at ambient pressure for runs #5 and #10. To account for the flow restrictions in the plenum, orifice and throttle valve, additional simulations were conducted with new boundary conditions at the mixing section outlet. For runs #2 and #6 the mixing section outlet boundary condition was changed to a setting in which Fluent varied the outlet pressure to match a user defined outlet mass flow rate. It was noted by Gilbert and Hill that the integrated mass flow rate had significant error therefore, the final simulations were conducted using the mass flow rates measured at the orifice for runs #2 and #6 which were 0.320 and 0.417 lb/s*in respectively.

2.2.4 Numerical Solution Techniques

The implicit solver in Fluent is employed to solve the RANS equations since it allows large time steps and the scheme is unconditionally stable [2]. The second-order Roe flux difference splitting (FDS) scheme is used for spatial discretization. The second order upwind spatial discretization was used in all simulations with the exception of the use of 3rd order MUSCL scheme with the SAS-SST k-ω turbulence model. To begin each simulation, a Courant number of 1 was used which was increased in steps as the solution converged in order to decrease the computational time

required. The solution was considered converged when the residuals of all flow variables reduced by three to six orders of magnitude and the mass flow rate of the mixing section outlet reached a steady state value.

2.3 Post Processing of the Solution

After the simulations converged, the velocity profile data, mixing section wall static pressure and centerline velocity were exported from Fluent for post-processing. This data was then imported into Microsoft Excel and plotted against the experimental data.

3 Results

This chapter compares the simulation results with two different inlet/outlet boundary conditions and with the experimental data. The results that are compared consist of the mass flow rates, mixing section wall static pressure, centerline velocity, and the velocity profiles in the mixing section. In general, computations agree reasonably well with the experimental data; however the degree of discrepancy between the computations and the experiment depends upon the turbulence model used in the calculation.

3.1 Effect of Boundary Conditions on Mass Flow Rates

In the computations, using the experimental nozzle pressure as the boundary condition at the nozzle inlet resulted in the calculated mass flow rate being higher than the experimental results except for runs #1 and #10. These runs involved the mixing section being open to the ambient atmosphere, with least restriction to the flow. Table 3.1 shows the mass flow rates for the experimental conditions as well as for each computed solution.

Table 3.1 Comparison of Mass Flow Rates using the Pressure Boundary Conditions.

Run #	Experiment Nozzle Flow Rate lb/s-in	Calculated Nozzle Flow Rate lb/s-in	Experiment Mixing Section Flow lb/s-in	Calculated Mixing Section Flow Rate lb/s-in				
				SA	k-ε	SST k-ω	Transition SST	SAS-SST k-ω
1	0.0780	0.0801	0.408	0.421	0.418	0.393	0.392	0.384
2	0.0782	0.0801	0.341	0.417	0.414	0.390	0.389	0.384
3	0.0750	0.0801	0.357	0.417	0.414	0.390	0.389	0.386
5	0.0787	0.0797	0.384	0.418	0.400	0.394	0.402	0.371
6	0.0882	0.0809	0.434	0.538	0.530	0.495	0.494	0.485
7	0.0884	0.0883	0.458	0.541	0.532	0.496	0.496	0.483
9	0.0884	0.0882	0.501	0.532	0.519	0.490	0.494	0.484
10	0.0874	0.0871	0.525	0.531	0.515	0.491	0.490	0.487

It can be noted from Table 3.1 that using a pressure boundary condition at the nozzle inlet results in a computed mass flow rate higher than the experimental flow rate for case 1 and slightly lower than the experimental value for case 2. Since the use of pressure boundary condition causes the simulations to differ from the experiment, the computed mixing section mass flow rate cannot be to meaningfully compared to the experimental results. Nevertheless, it can be seen from Table 3.1 that

for a given run, the mixing section flow rate is greatest when using the SA model and decreases with the use of *k-ε*, SST *k-ω*, Transition SST, and SAS-SST *k-ω* turbulence models in that order. After changing the nozzle inlet and mixing section outlet boundary conditions by specifying the mass flow rate at the nozzle exit, the mass flow rates were again computed and the results are shown in Table 3.2. For case 1, with a 1.25 inch wide throat, run #5 had no flow restriction and run #2 had the maximum flow restriction. For case 2, with a 1.875 inch wide throat, run #10 had no flow restriction and run #6 had the maximum flow restriction.

Table 3.2: Comparison of Mass Flow Rates using the Mass Flow Boundary Condition at the Nozzle Exit.

Run #	Experiment Nozzle Flow Rate lb/s-in	Calculated Nozzle Flow Rate lb/s-in	Experimental Mixing Section Flow Rate lb/s-in	Calculated Mixing Section Flow Rate lb/s-in				
				SA	k-ε	SST k-ω	Transitio n SST	SAS-SST k-ω
2	0.0782	0.0782	0.322	0.325	0.325	0.325	0.325	0.325
5	0.0787	0.0787	0.395	0.414	0.397	0.390	0.384	0.380
6	0.0882	0.0882	0.420	0.417	0.417	0.417	0.417	0.417
10	0.0874	0.0874	0.508	0.532	0.517	0.492	0.492	0.480

It can be seen from Table 3.2 that for runs #5 and #10, the best computational results are obtained when using the SST *k-ω* turbulence model. For these two runs the mixing section outlet was set to zero gage pressure. In runs #2 and #6, Fluent solved for an outlet pressure that corresponded to an input mass flow rate so that there was no difference in the mass flow rate results at the inlet and the outlet.

3.2 Mixing Section Wall Static Pressure

The computational results for the mixing section wall static pressure varied in a similar fashion as the experimental data, that is the slope of the static pressure followed that in the experiment; however the magnitude of the static pressure varied depending upon the turbulence model employed in the computation as can be seen from Figure 3.1-3.12. Runs #1 and #5 match with the experimental data quite well as can be seen from Figures 3.1 and 3.4 using the SAS-SST *k-ω* and SST *k-ω* models respectively. However, the agreement worsens for SA and *k-ε* models. In general, it can be seen from all the Figures 3.1-3.12 that the SA and *k-ε* models have the worst agreement with the experimental data.

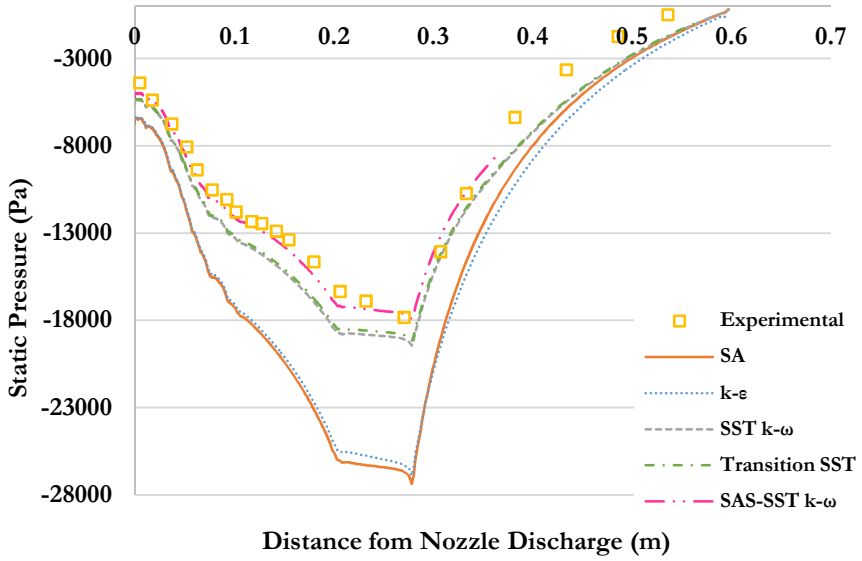

Figure 3.1 Run #1: Comparison of Computed Wall Static Pressure Distribution using Various Turbulence Models and the Experimental Data.

Figures 3.2 and 3.3 show that for runs #2 and #3, static pressure has a similar trend in variation as in the experimental data; however the computed values are much lower than the experimental values using all the turbulence models. This can be explained that this discrepancy is due to the fact that the downstream restrictions were not used in the computations. Again the computed results using the SAS-SST k-ω and SST k-ω models are much closer to the experimental data than any other model.

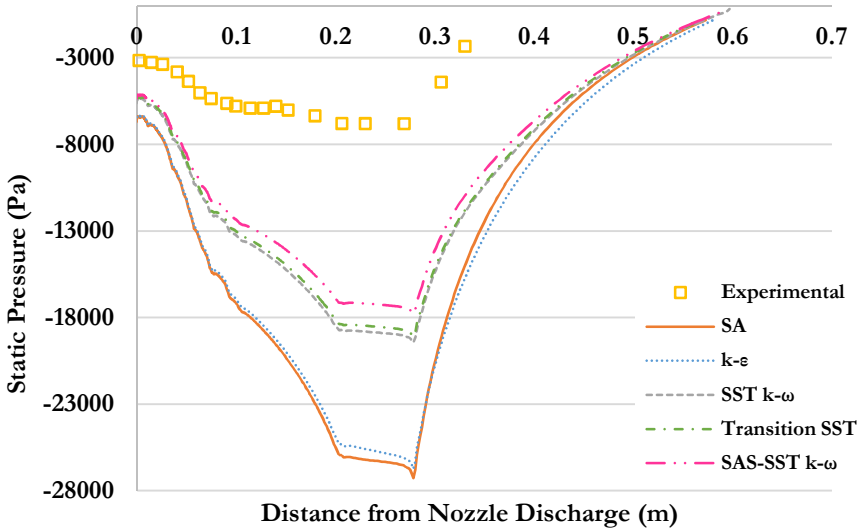

Figure 3.2 Run #2: Comparison of Computed Wall Static Pressure Distribution using Various Turbulence Models and the Experimental Data.

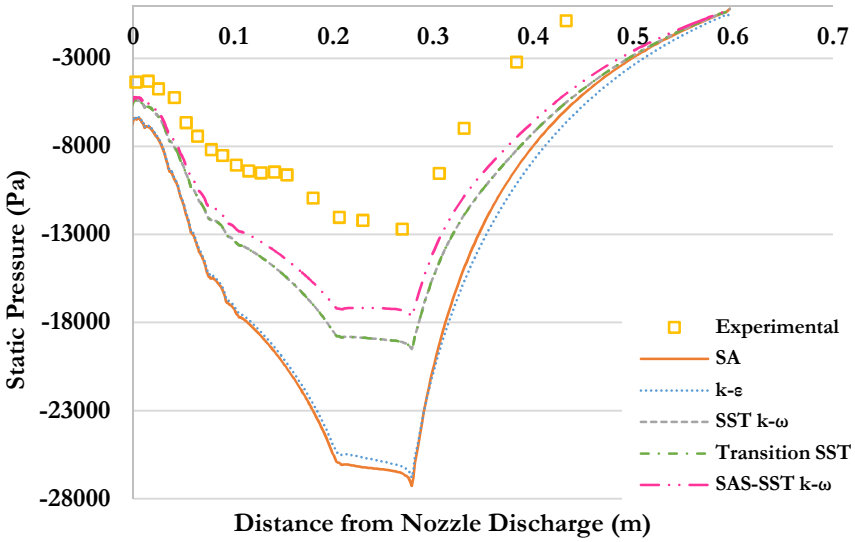

Figure 3.3 Run #3: Comparison of Computed Wall Static Pressure Distribution using Various Turbulence Models and the Experimental Data.

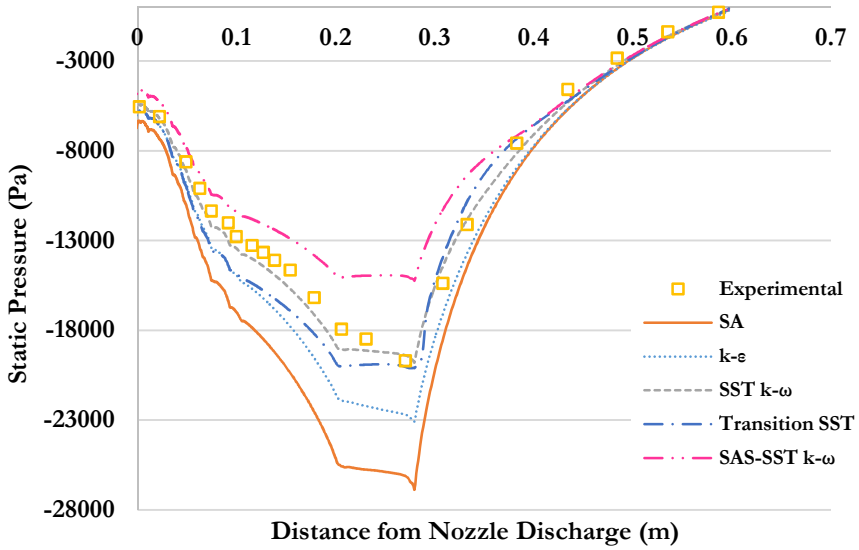

Figure 3.4 Run #5: Comparison of Computed Wall Static Pressure Distribution using Various Turbulence Models and the Experimental Data.

The computed results for the 1.875" mixing section throat again agree quite well with the experimental data as far as changes in the static pressure downstream of the nozzle are concerned. Runs #6 and #7 had the large flow restrictions connected to the mixing section in the experiment,

as a result Figures 3.5 and 3.6 show lower computed static pressure since the restrictions were not accounted for in the boundary conditions in the computations.

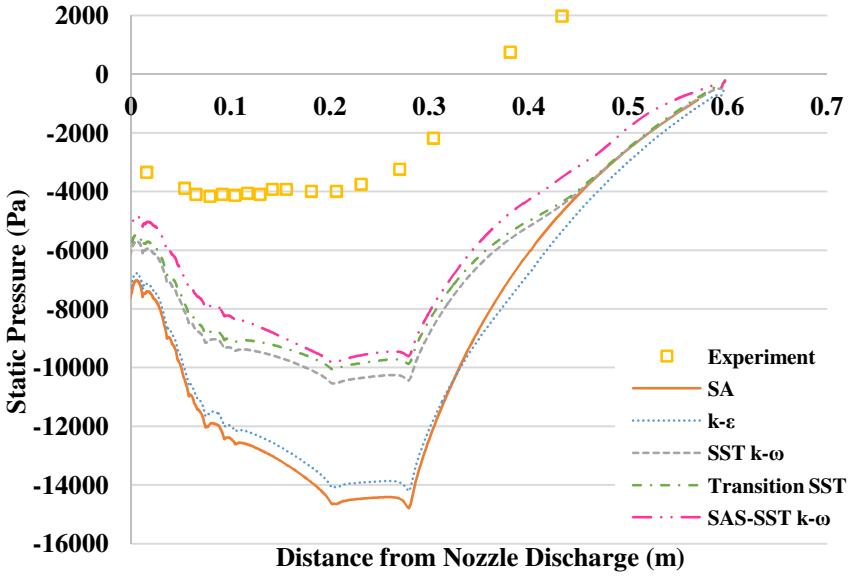

Figure 3.5 Run #6: Comparison of Computed Wall Static Pressure Distribution using Various Turbulence Models and the Experimental Data.

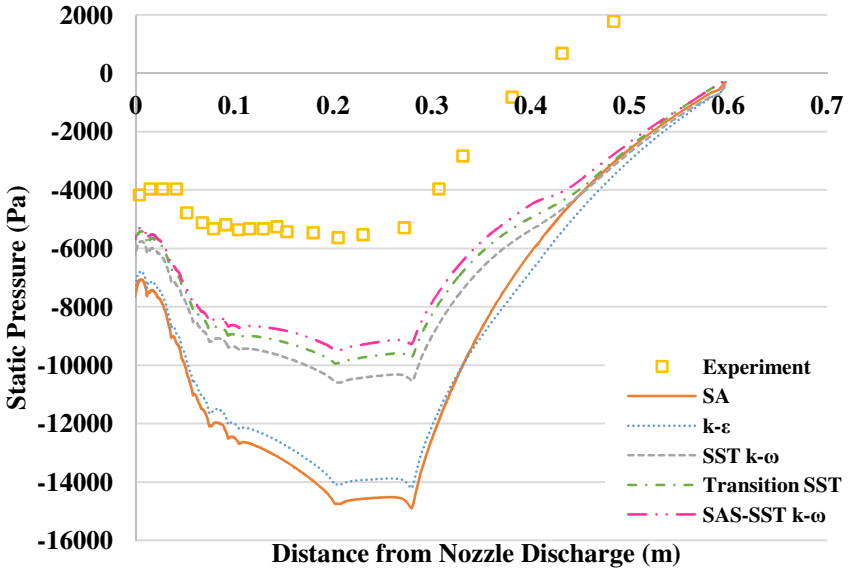

Figure 3.6 Run #7: Comparison of Computed Wall Static Pressure Distribution using Various Turbulence Models and the Experimental Data.

For the 1.857" mixing section throat, all four simulations show that the SA and *k-ε* turbulence models are reasonably accurate. However, the use of the Transition SST model with 3rd order accurate numerical scheme and the SAS-SST *k-ω* model yield the best results. It should be noted however that in runs #9 and #10, these two models give higher static pressure in the narrowest part of the mixing section as shown in Figures 3.7 and 3.8.

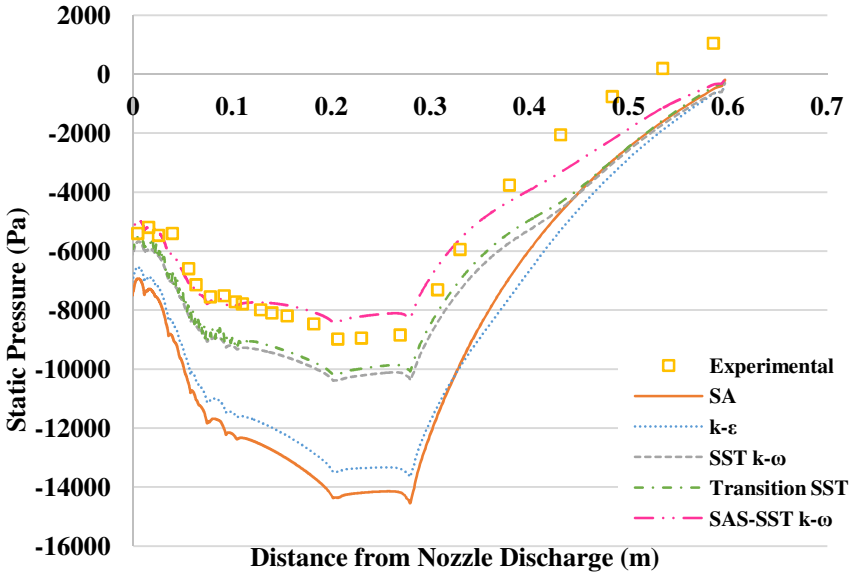

Figure 3.7 Run #9: Comparison of Computed Wall Static Pressure Distribution using Various Turbulence Models and the Experimental Data.

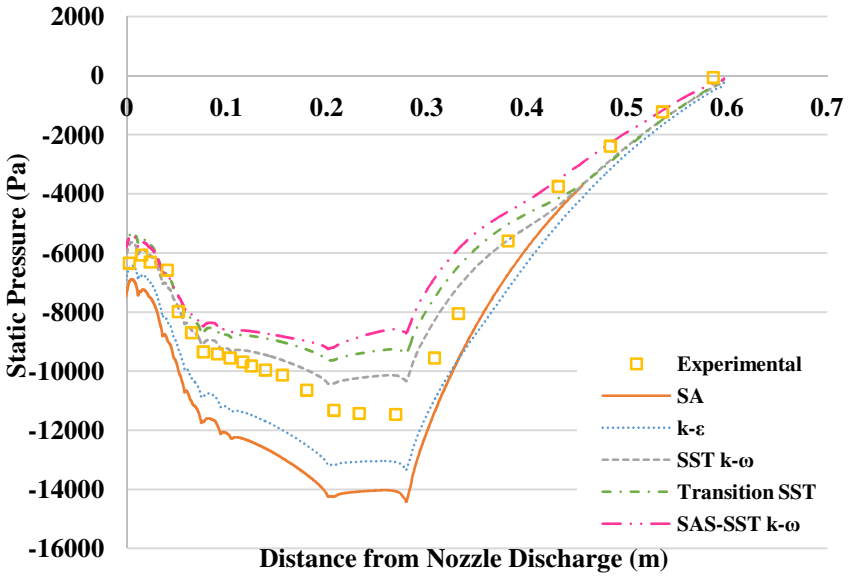

Figure 3.8 Run #10: Comparison of Computed Wall Static Pressure Distribution using Various Turbulence Models and the Experimental Data.

The computed results for the mixing section wall static pressure obtained by employing the pressure boundary conditions do not show good agreement with the experimental data. These results however do show how the use of a particular turbulence model affects the magnitude of the static pressure at the wall. The computed results obtained by applying the mass flow rate boundary condition at the nozzle inlet and varying the pressure at the ejector outlet are shown in Figures 3.9-3.12. The mixing section wall static pressures for runs #2, #5, #6, and #10 were computed using this boundary condition.

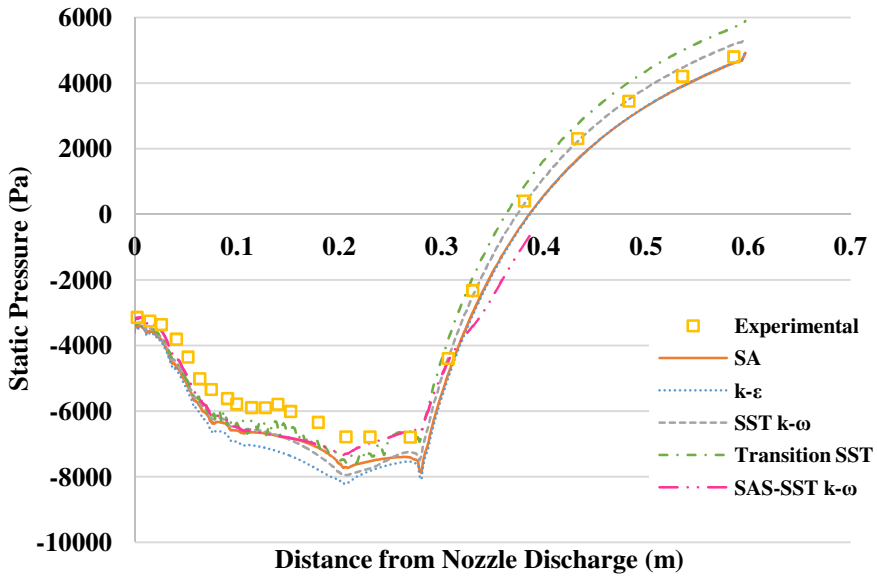

Figure 3.9 Run #2: Comparison of Computed Wall Static Pressure using various Turbulence Models with Mass Flow Rate Boundary Condition, with the Experimental Data.

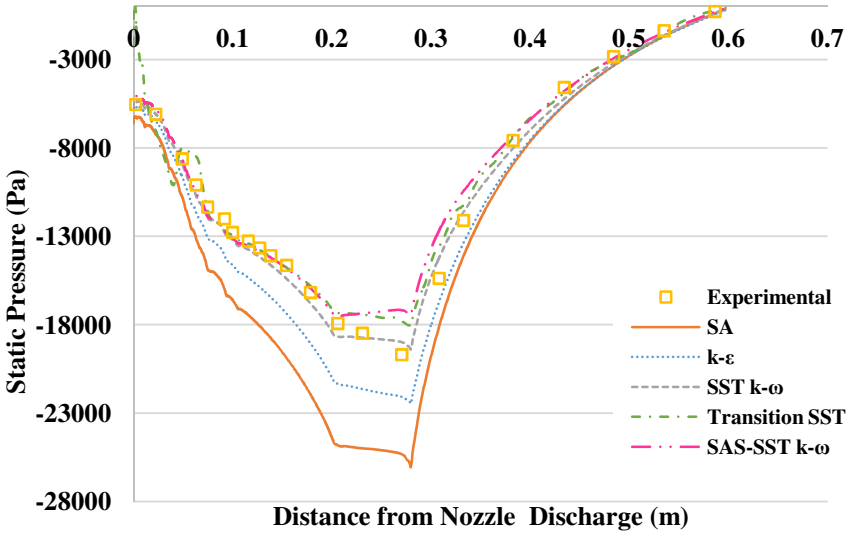

Figure 3.10 Run #5: Comparison of Computed Wall Static Pressure using various Turbulence Models with Mass Flow Rate Boundary Condition, with the Experimental Data.

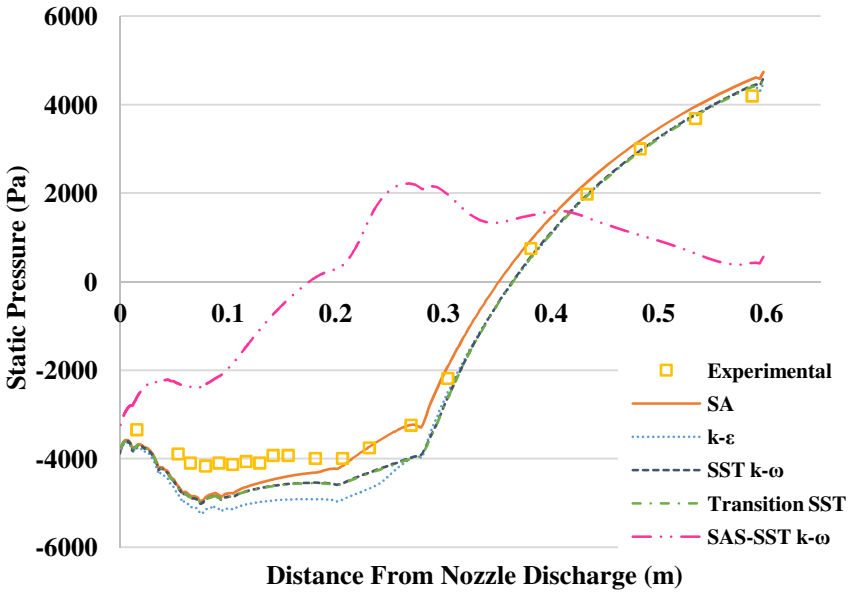

Figure 3.11 Run #6: Comparison of Computed Wall Static Pressure using various Turbulence Models with Mass Flow Rate Boundary Condition, with the Experimental Data.

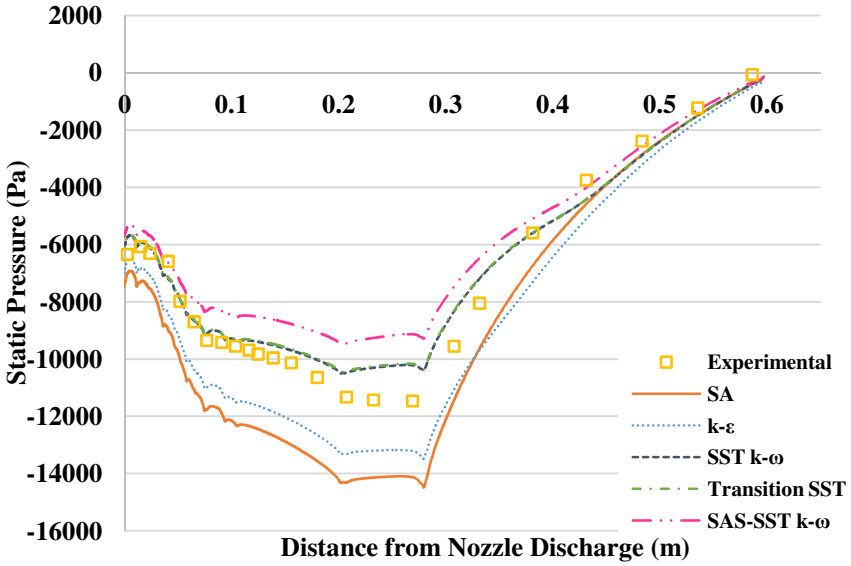

Figure 3.12 Run #10: Comparison of Computed Wall Static Pressure using various Turbulence Models with Mass Flow Rate Boundary Condition, with the Experimental Data.

3.3 Variation in Centerline Velocity along the Nozzle-Ejector Axis

The computed centerline velocity results show similar variations using different turbulence models as in the static wall pressure results in section 3.2, when compared with the experimental data. Like before in section 3.2, the SA and k-ε models produce results with the greatest deviation from the experimental data as shown in figures 3.13-3.16. However, figures 3.13 – 3.16 also show that the remaining three models produce results closer to the data with little difference among them.

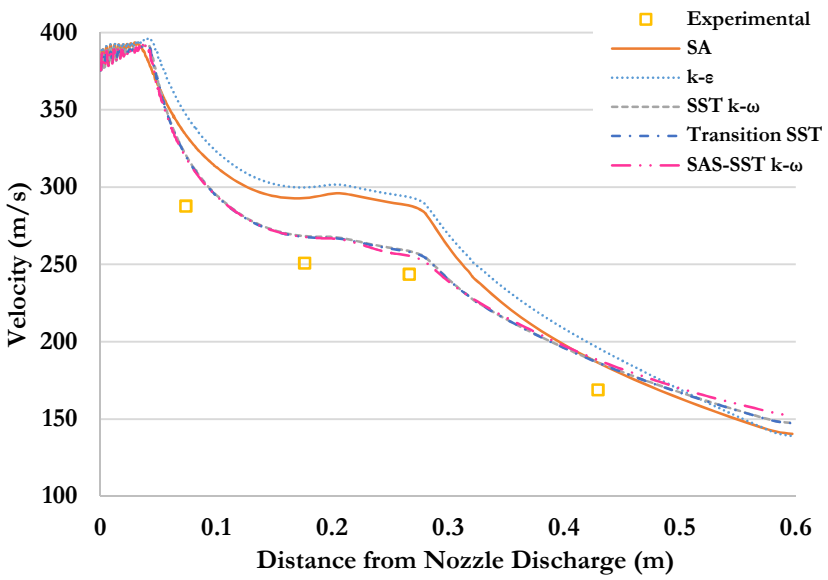

Figure 3.13 Run #1: Comparison of Computed Centerline Velocity using various Turbulence Models with the Experimental Data.

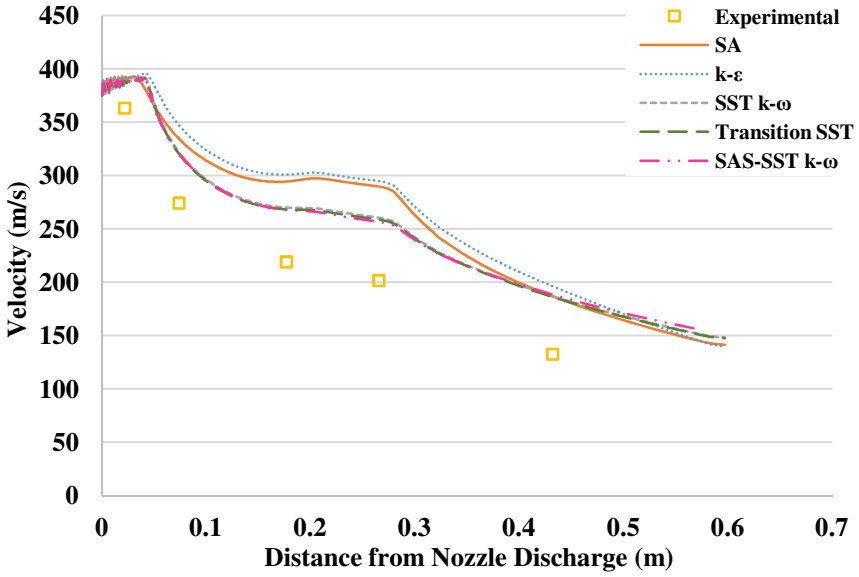

Figure 3.14 Run #2: Comparison of Computed Centerline Velocity using various Turbulence Models with the Experimental Data.

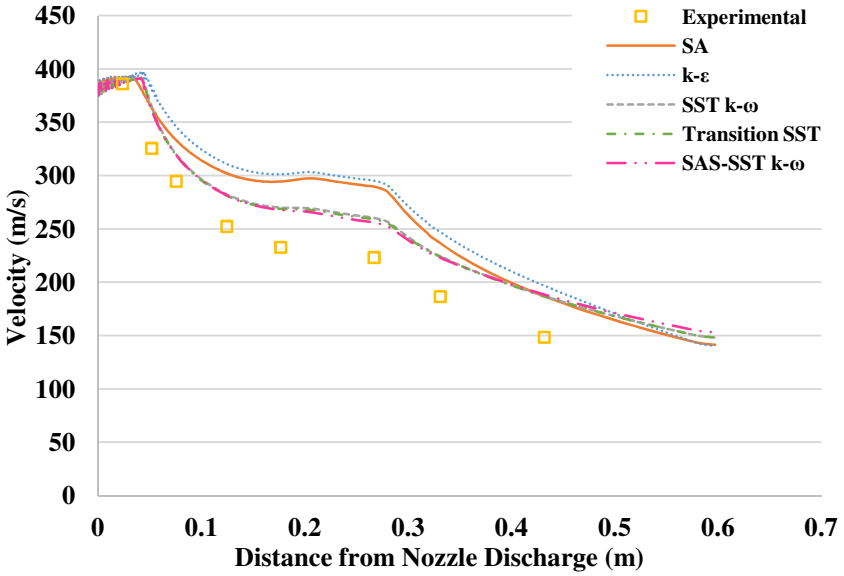

Figure 3.15 Run #3: Comparison of Computed Centerline Velocity using various Turbulence Models with the Experimental Data.

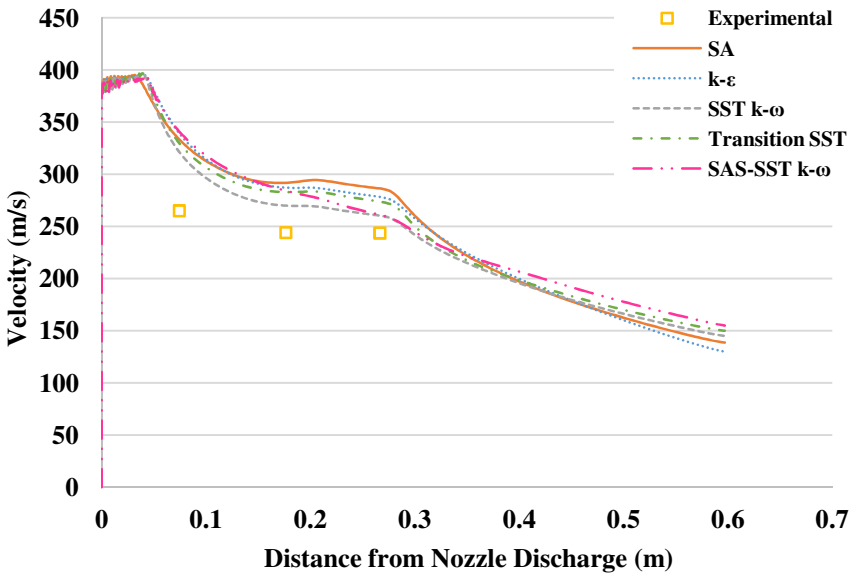

Figure 3.16 Run #5: Comparison of Computed Centerline Velocity using various Turbulence Models with the Experimental Data.

For the 1.875" mixing section throat simulations, Figures 3.17-3.20 show that all of the turbulence models produce good results again with the exception of the SA and *k-ε* models, when compared to the experimental data.

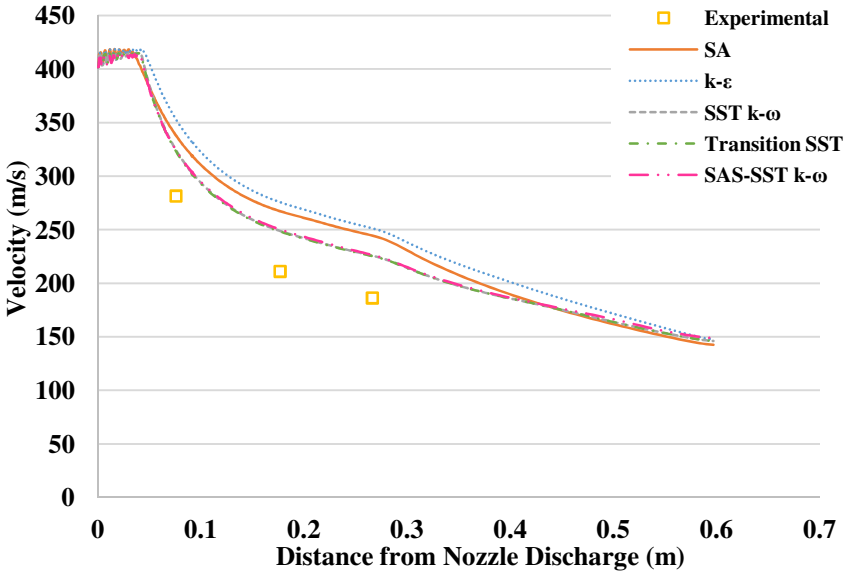

Figure 3.17 Run #6: Comparison of Computed Centerline Velocity using various Turbulence Models with the Experimental Data.

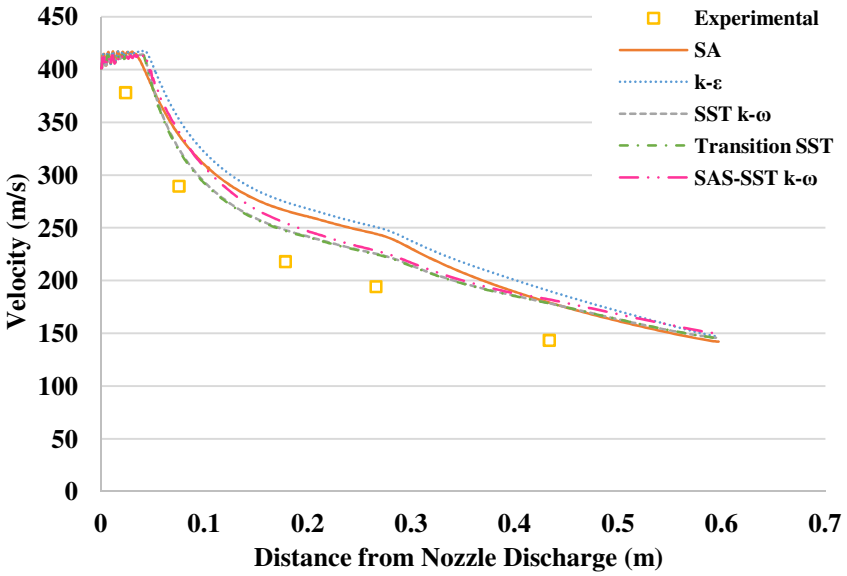

Figure 3.18 Run #7: Comparison of Computed Centerline Velocity using various Turbulence Models with the Experimental Data.

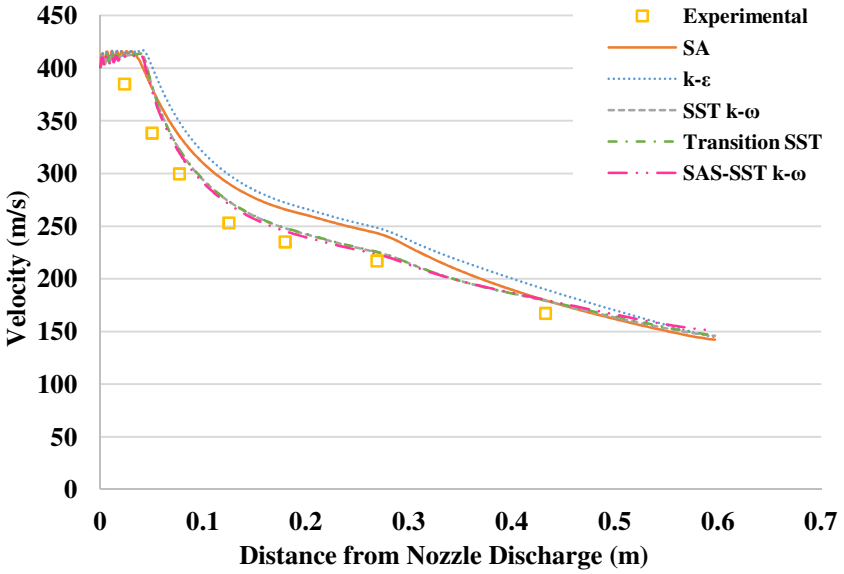

Figure 3.19 Run #9: Comparison of Computed Centerline Velocity using various Turbulence Models with the Experimental Data.

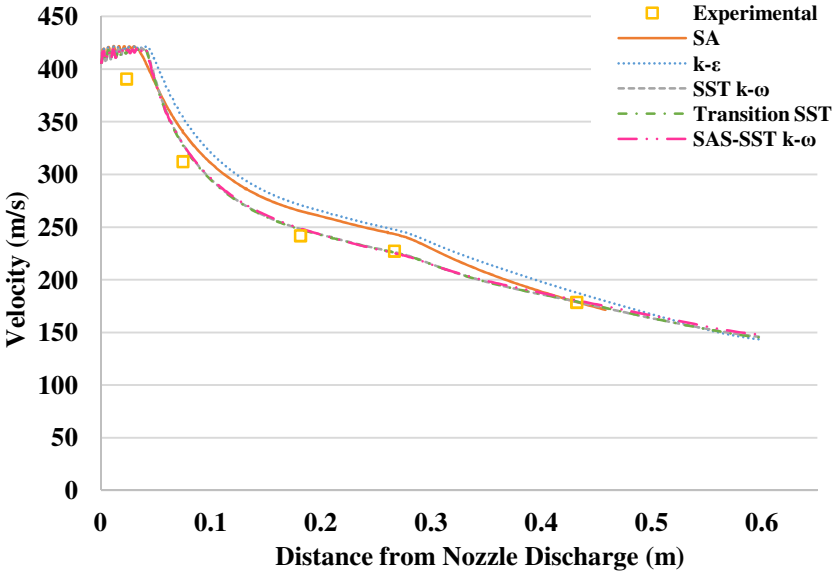

Figure 3.20 Run #10: Comparison of Computed Centerline Velocity using various Turbulence Models with the Experimental Data.

The above results show that there is little difference between the computed centerline velocities when using the SST *k-ω*, Transition SST, and SAS-SST *k-ω* turbulence models. The SA and *k-ε* models produce higher velocity magnitudes along the centerline in the region of approximately 4 to 16 inches downstream of the nozzle, which is an area of high rate of dissipation

of turbulent kinetic energy. Figures 3.21-3.24 show the comparison of computed centerline velocity with the experimental data when using the mass flow rate boundary condition at the nozzle inlet. The difference in results using various turbulence models is similar to the previous results when compared to t the experimental data. Overall the results show that the SST and Transition SST model consistently produce best results against the experimental results.

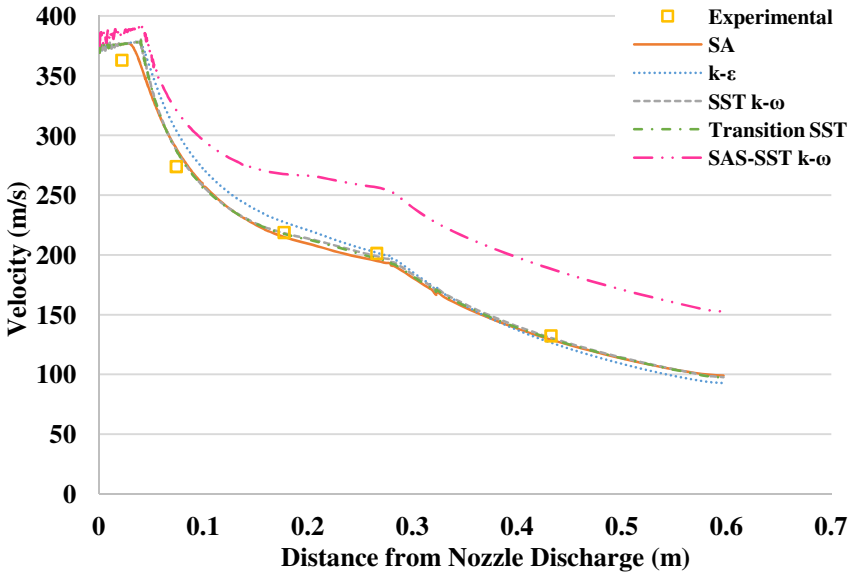

Figure 3-21 Run #2: Comparison of Centerline Velocity Profiles using Various Turbulence Models with Mass Flow Rate Boundary Conditions, with the Experimental Data.

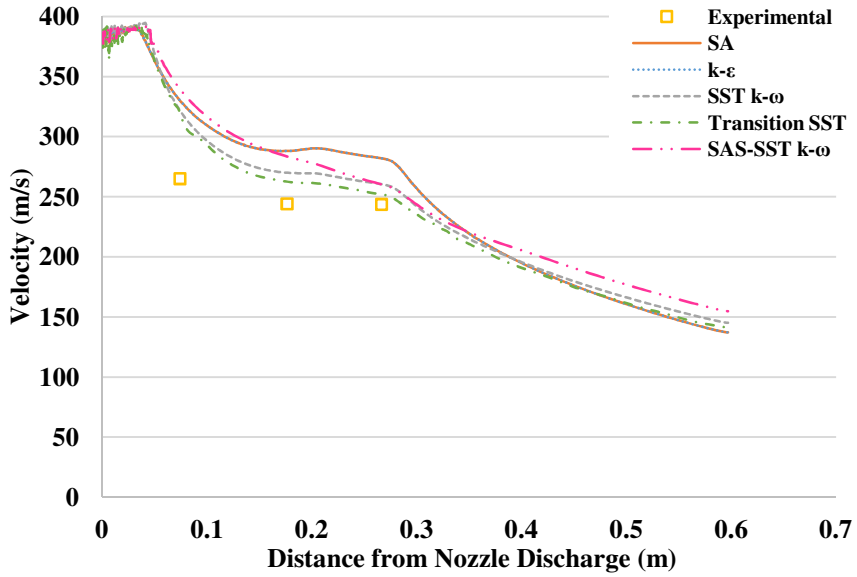

Figure 3-22 Run #5: Comparison of Centerline Velocity Profiles using Various Turbulence Models with Mass Flow Rate Boundary Conditions, with the Experimental Data.

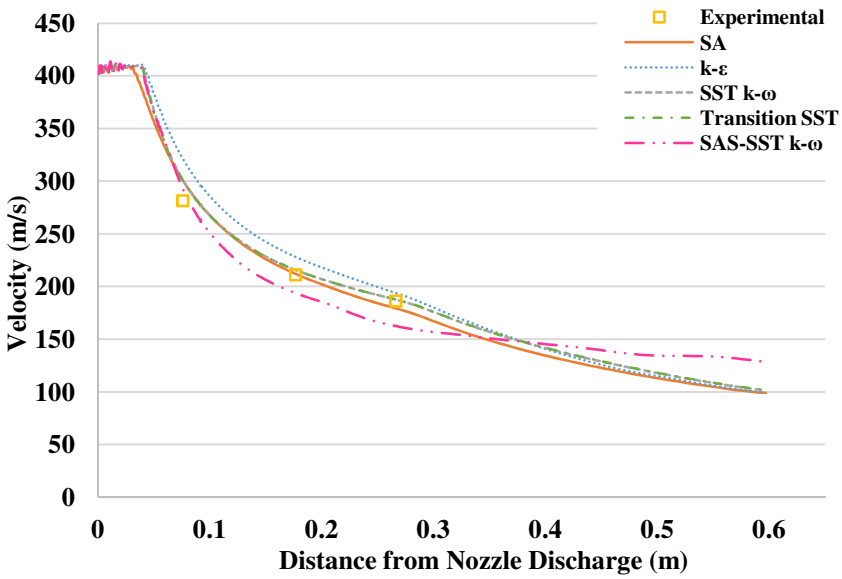

Figure 3-23 Run #6: Comparison of Centerline Velocity Profiles using Various Turbulence Models with Mass Flow Rate Boundary Conditions, with the Experimental Data.

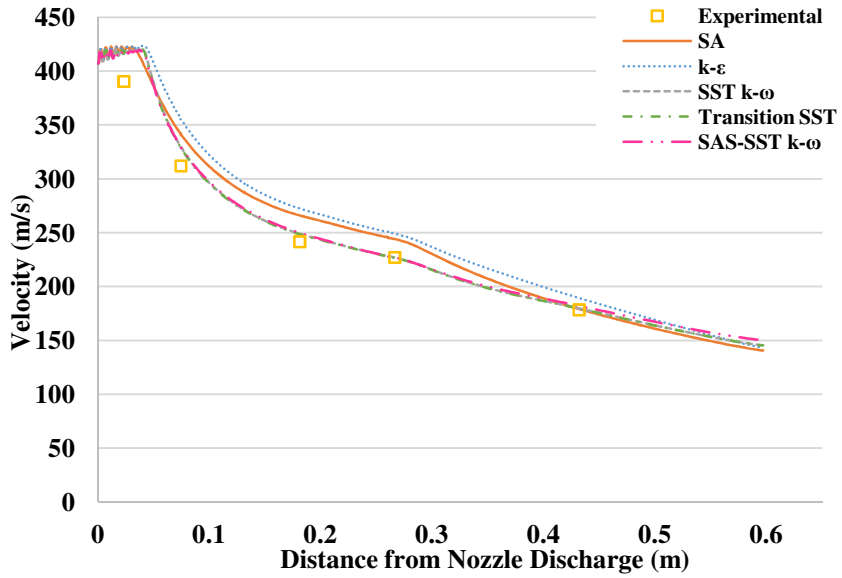

Figure 3-24 Run #10: Comparison of Centerline Velocity Profiles using Various Turbulence Models with Mass Flow Rate Boundary Conditions, with the Experimental Data.

3.4 Velocity Profiles at Various Cross-Sections of Nozzle-Ejector Configuration

The computed velocity profiles downstream of the nozzle matched quite well with the experimental data using different turbulence models. However, there are some differences in the computed results and the experimental data, some of it can be attributed to the boundary conditions in the computations not exactly matching with those in the experiment. Figures 3.25 - 3.28 show the comparison of the computed velocity profiles for run #1 with the experimental data.

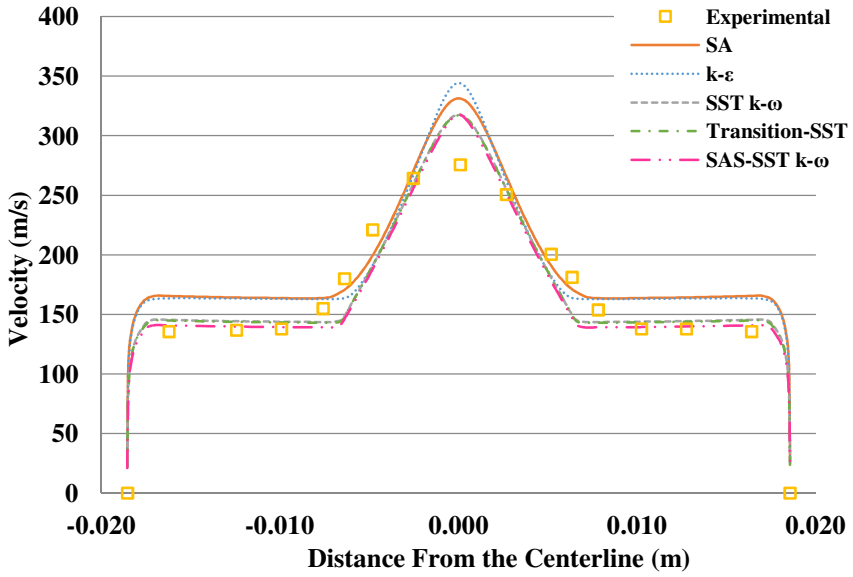

Figure 3.25 Run #1: Comparison of Velocity Profiles Computed using Various Turbulence Models with the Experimental Data at a Distance of 3 inches from the Nozzle Outlet.

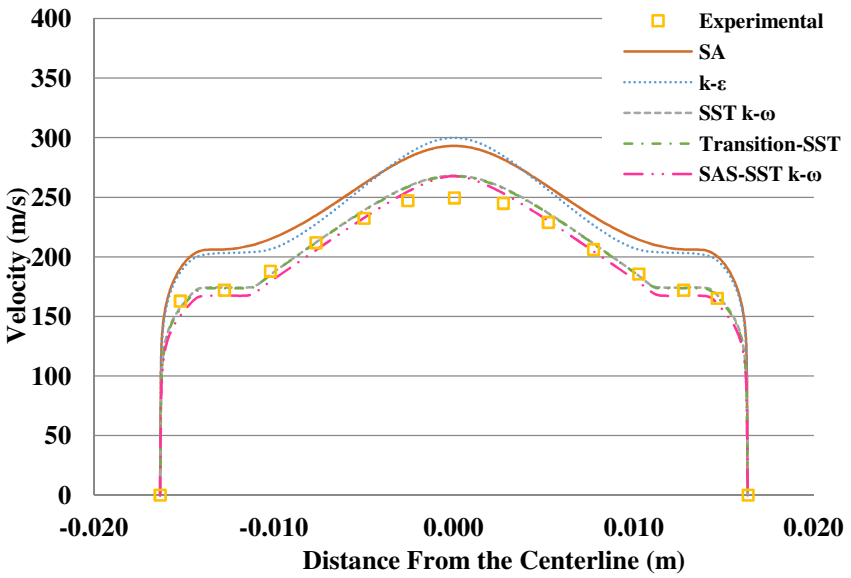

Figure 3.26 Run #1: Comparison of Velocity Profiles Computed using Various Turbulence Models with the Experimental Data at a Distance of 7 inches from the Nozzle Outlet.

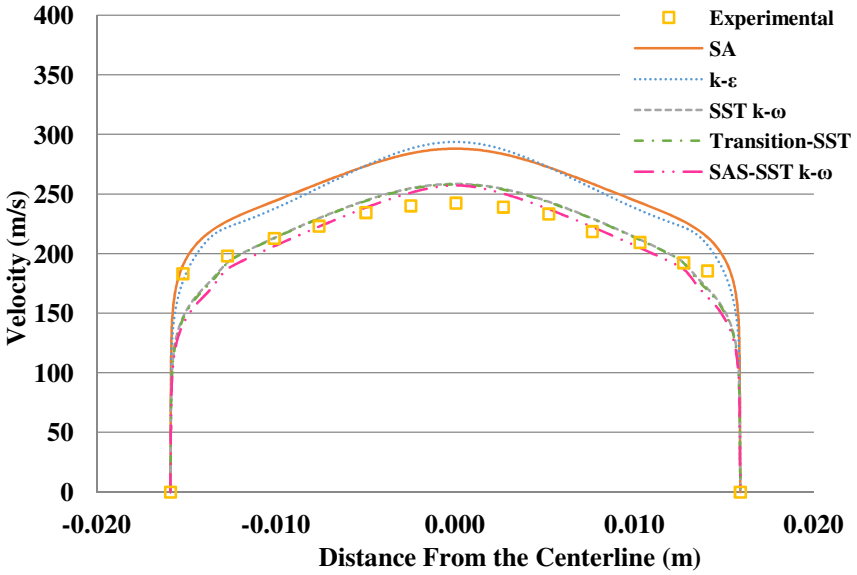

Figure 3.27 Run #1: Comparison of Velocity Profiles Computed using Various Turbulence Models with the Experimental Data at a Distance of 10.5 inches from the Nozzle Outlet.

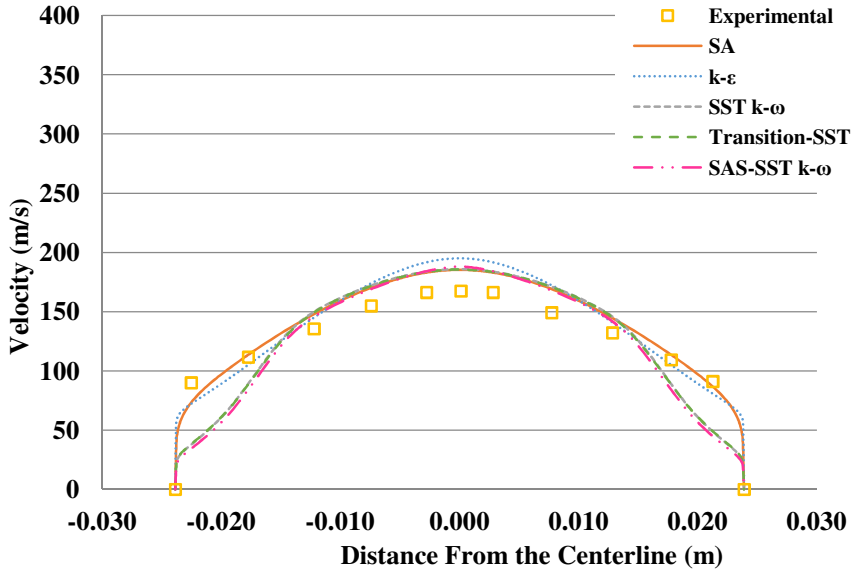

Figure 3.28 Run #1: Comparison of Velocity Profiles Computed using Various Turbulence Models with the Experimental Data at a Distance of 17 inches from the Nozzle Outlet.

Run #2 was one of the experimental tests that had flow restrictions to reduce the net mass flow rate. Since the mixing section outlet was modeled in the computations as a pressure outlet with pressure equal to the ambient pressure, the results show a higher mass flow rate and velocity than observed by Gilbert and Hill in the experiment. Figures 3.29-3.33 show the velocity profiles from simulation of run #2 and their comparison with the experiment.

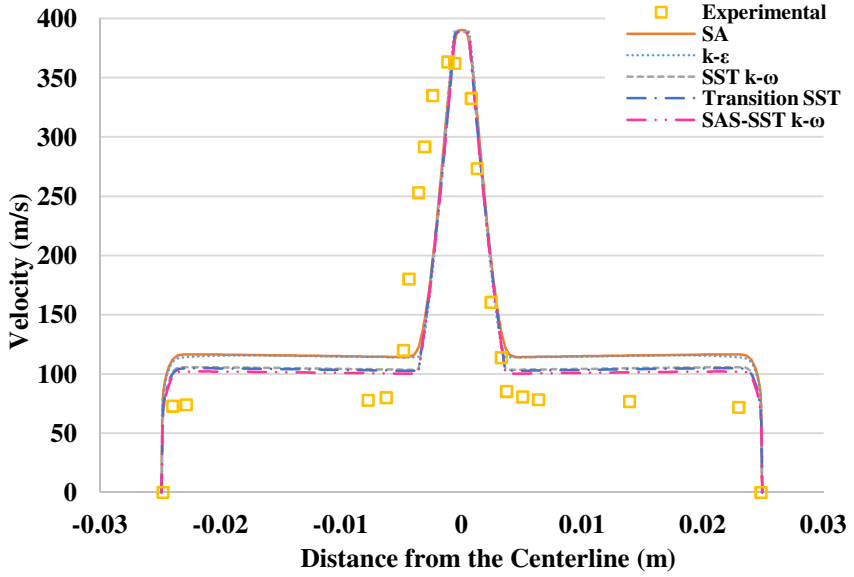

Figure 3.29 Run #2: Comparison of Velocity Profiles Computed using Various Turbulence Models with the Experimental Data at a Distance of 1 inch from the Nozzle Outlet.

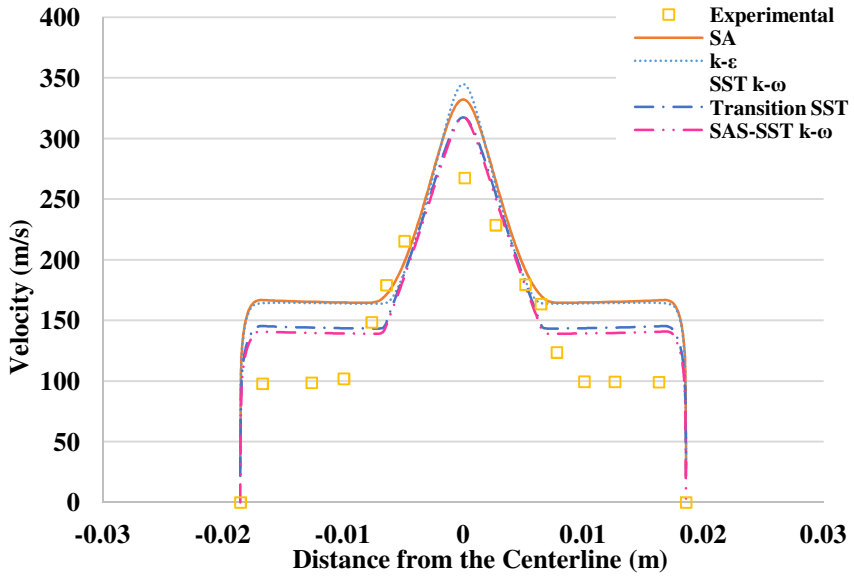

Figure 3.30 Run #2: Comparison of Velocity Profiles Computed using Various Turbulence Models with the Experimental Data at a Distance of 3 inches from the Nozzle Outlet.

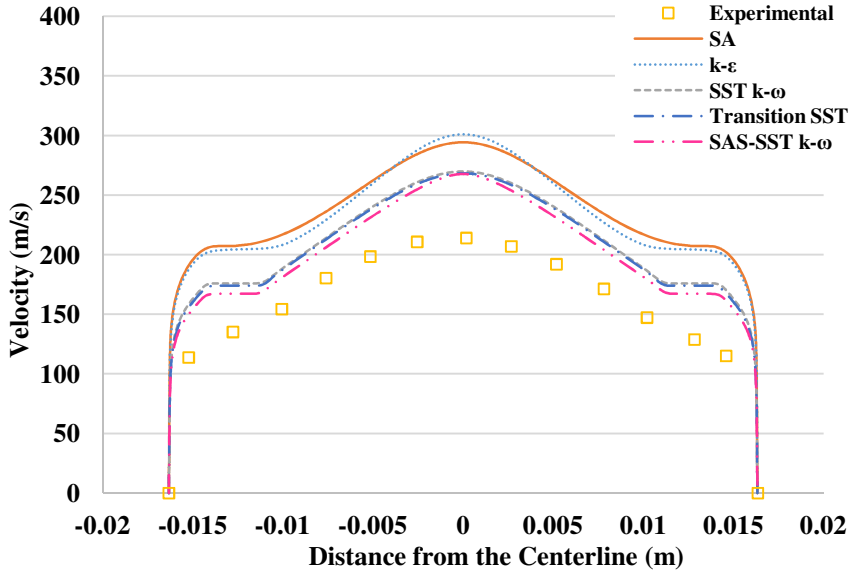

Figure 3.31 Run #2: Comparison of Velocity Profiles Computed using Various Turbulence Models with the Experimental Data at a Distance of 7 inches from the Nozzle Outlet.

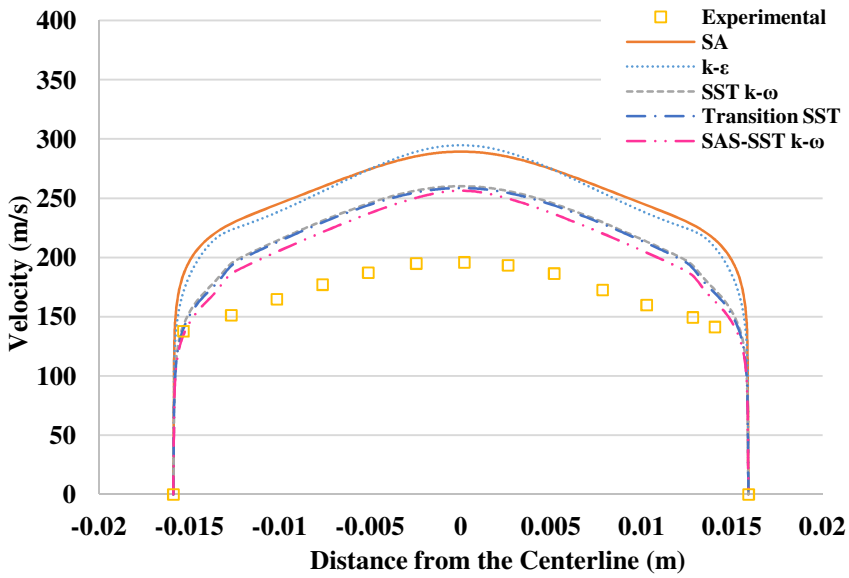

Figure 3.32 Run #2: Comparison of Velocity Profiles Computed using Various Turbulence Models with the Experimental Data at a Distance of 10.5 inches from the Nozzle Outlet.

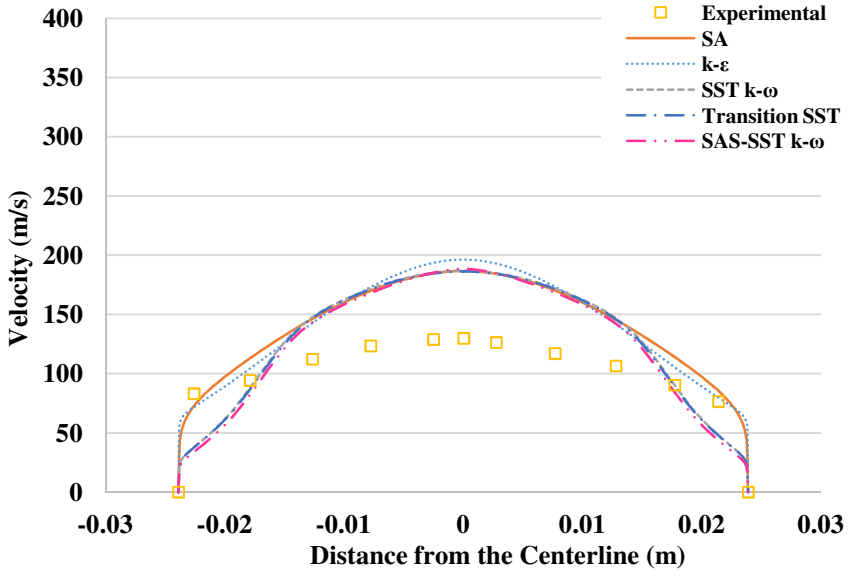

Figure 3.33 Run #2: Comparison of Velocity Profiles Computed using Various Turbulence Models with the Experimental Data at a Distance of 17 inches from the Nozzle Outlet.

The computed results for run #3 are shown in Figures 3.34-3.42. These figures show that close to the nozzle inlet, best comparison between the computations and the experimental data is obtained by using the SAS-SST *k-ω* model followed by the Transition SST and SST *k-ω* model. As

the momentum of the nozzle stream diffuses past the mixing section throat, the opposite becomes true with respect to the shape of the velocity profiles, all the simulation results tend to be higher in velocity magnitude than the experimental data near the end of the mixing section. This could also be due to the absence of any flow restrictions in the simulation boundary conditions.

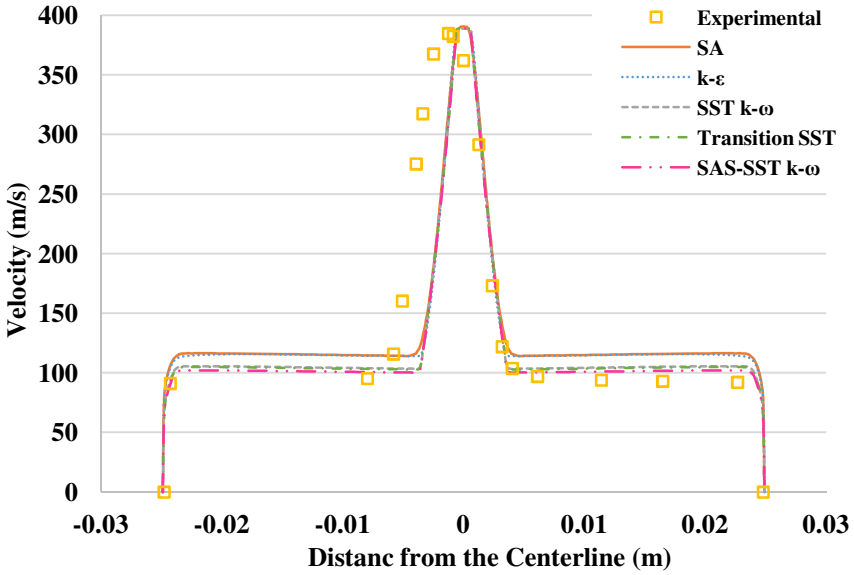

Figure 3.34 Run #3: Comparison of Velocity Profiles Computed using Various Turbulence Models with the Experimental Data at a Distance of 1 inch from the Nozzle Outlet.

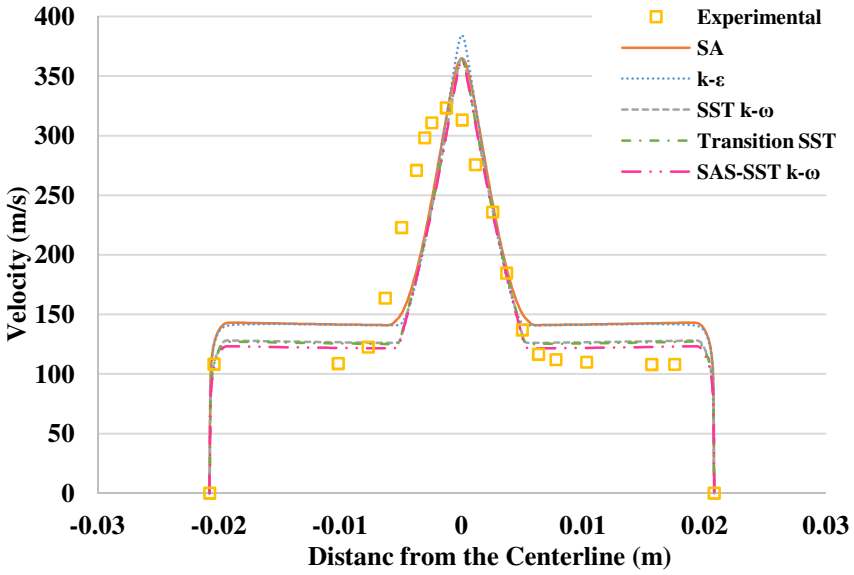

Figure 3.35 Run #3: Comparison of Velocity Profiles Computed using Various Turbulence Models with the Experimental Data at a Distance of 2 inches from the Nozzle Outlet.

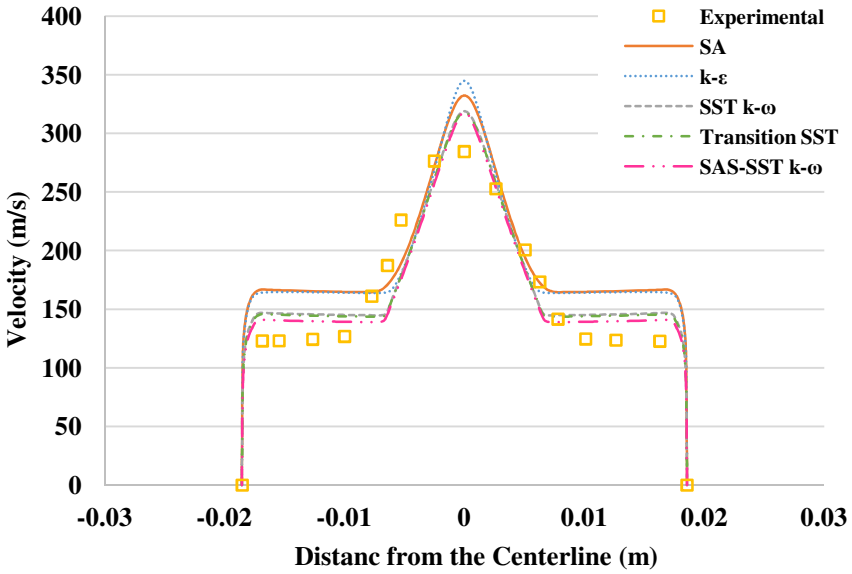

Figure 3.36 Run #3: Comparison of Velocity Profiles Computed using Various Turbulence Models with the Experimental Data at a Distance of 3 inches from the Nozzle Outlet.

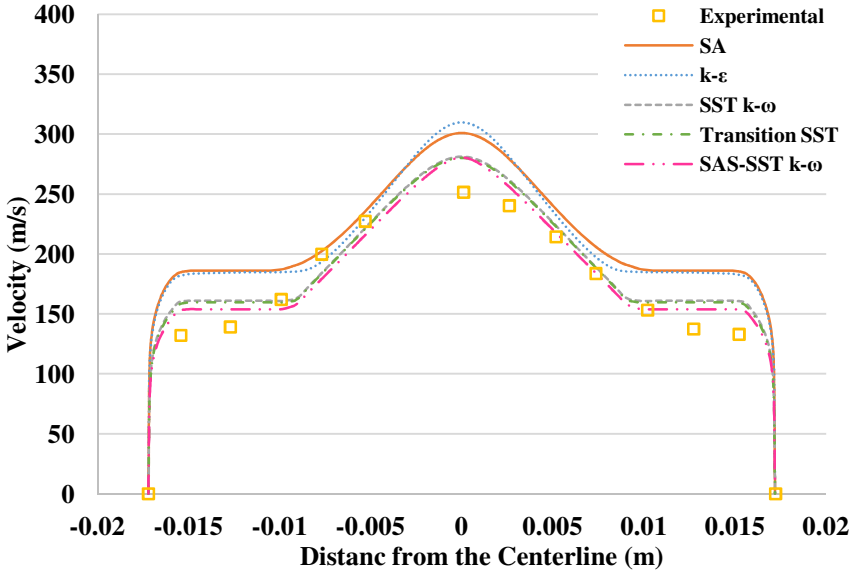

Figure 3.37 Run #3: Comparison of Velocity Profiles Computed using Various Turbulence Models with the Experimental Data at a Distance of 5 inches from the Nozzle Outlet.

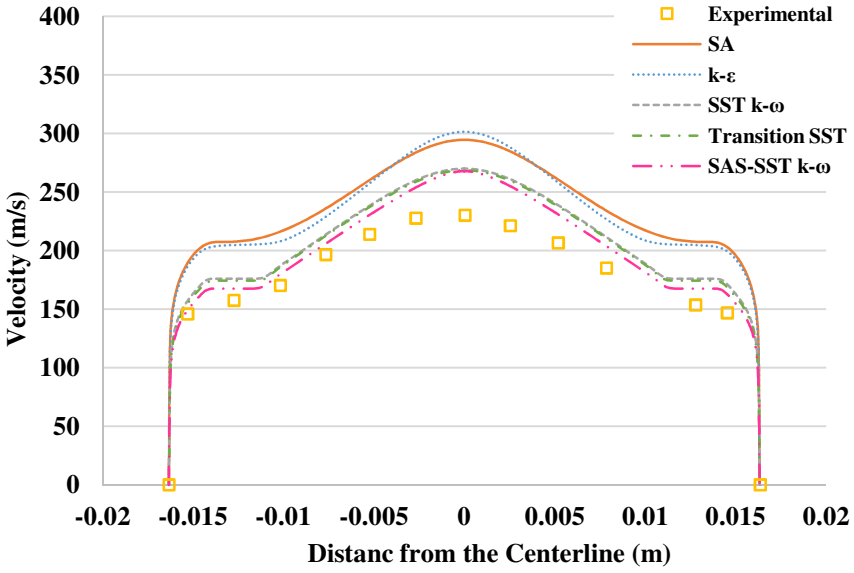

Figure 3.38 Run #3: Comparison of Velocity Profiles Computed using Various Turbulence Models with the Experimental Data at a Distance of 7 inches from the Nozzle Outlet.

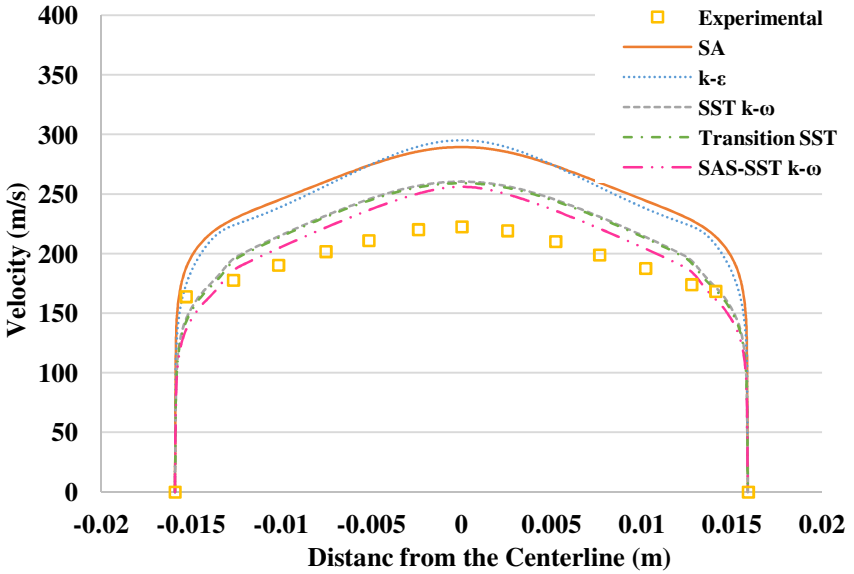

Figure 3.39 Run #3: Comparison of Velocity Profiles Computed using Various Turbulence Models with the Experimental Data at a Distance of 10.5 inches from the Nozzle Outlet.

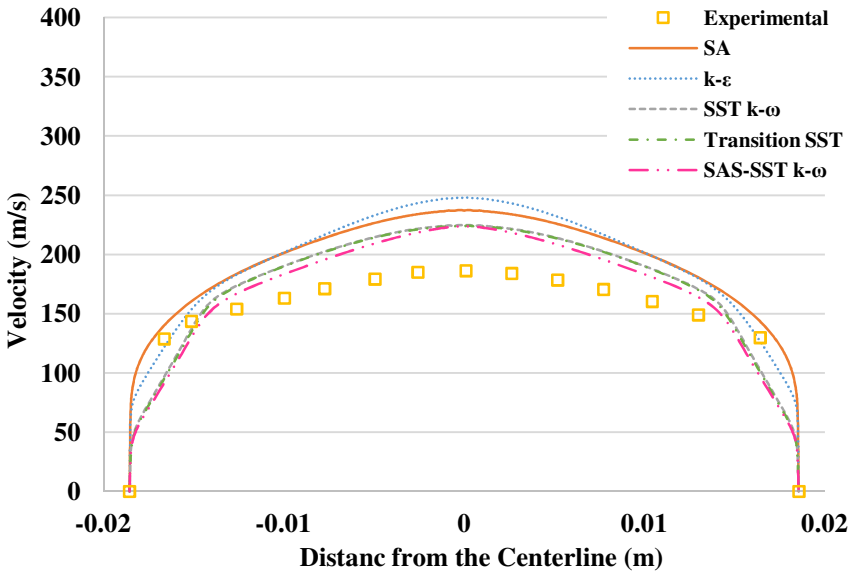

Figure 3.40 Run #3: Comparison of Velocity Profiles Computed using Various Turbulence Models with the Experimental Data at a Distance of 13 inches from the Nozzle Outlet.

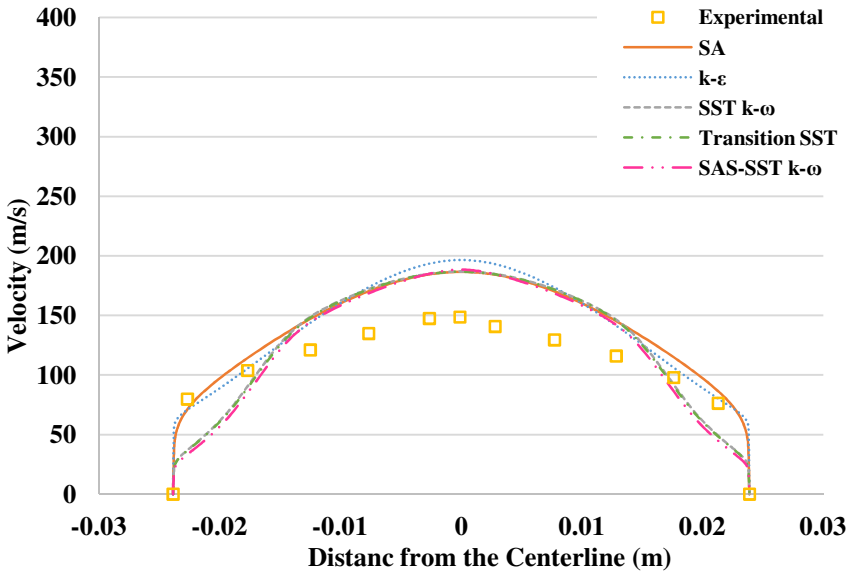

Figure 3.41 Run #3: Comparison of Velocity Profiles Computed using Various Turbulence Models with the Experimental Data at a Distance of 17 inches from the Nozzle Outlet.

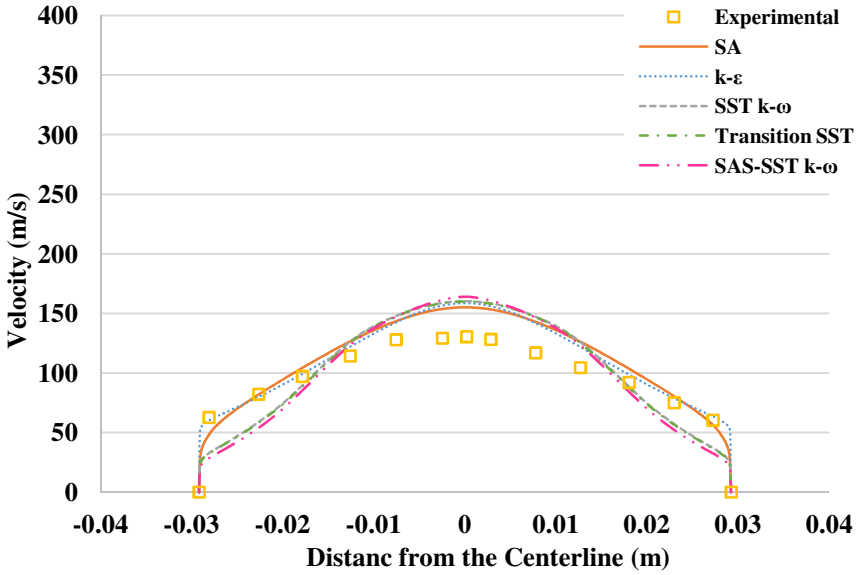

Figure 3.42 Run #3: Comparison of Velocity Profiles Computed using Various Turbulence Models with the Experimental Data at a Distance of 21 inches from the Nozzle Outlet.

The results of run #5 simulation are presented in Figures 3.43-3.45. These results are similar to those of run #1, both cases had no flow restriction after the mixing section outlet.

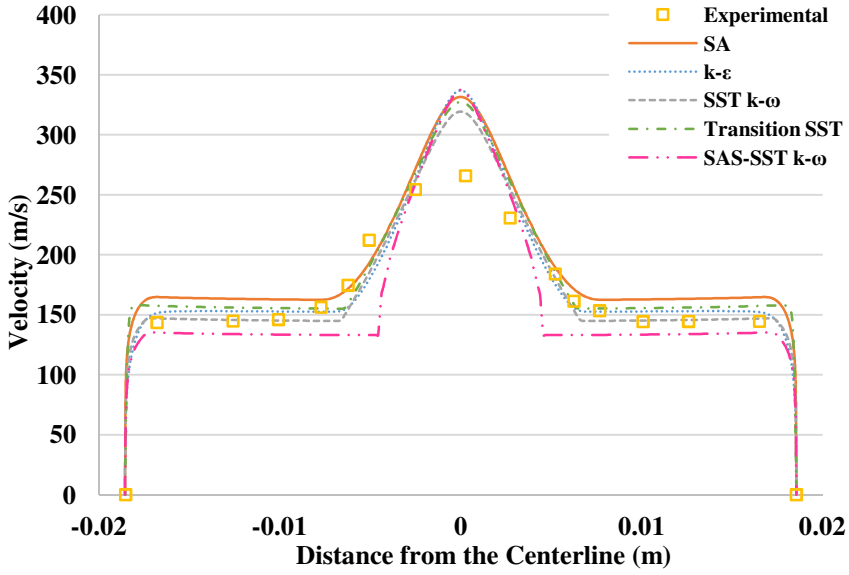

Figure 3.43 Run #5: Comparison of Velocity Profiles Computed using Various Turbulence Models with the Experimental Data at a Distance of 3 inches from the Nozzle Outlet.

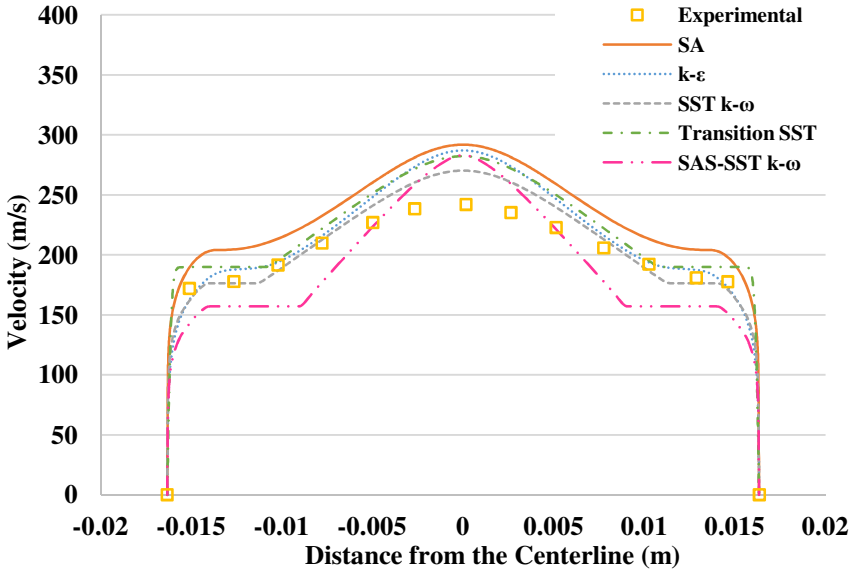

Figure 3.44 Run #5: Comparison of Velocity Profiles Computed using Various Turbulence Models with the Experimental Data at a Distance of 7 inches from the Nozzle Outlet.

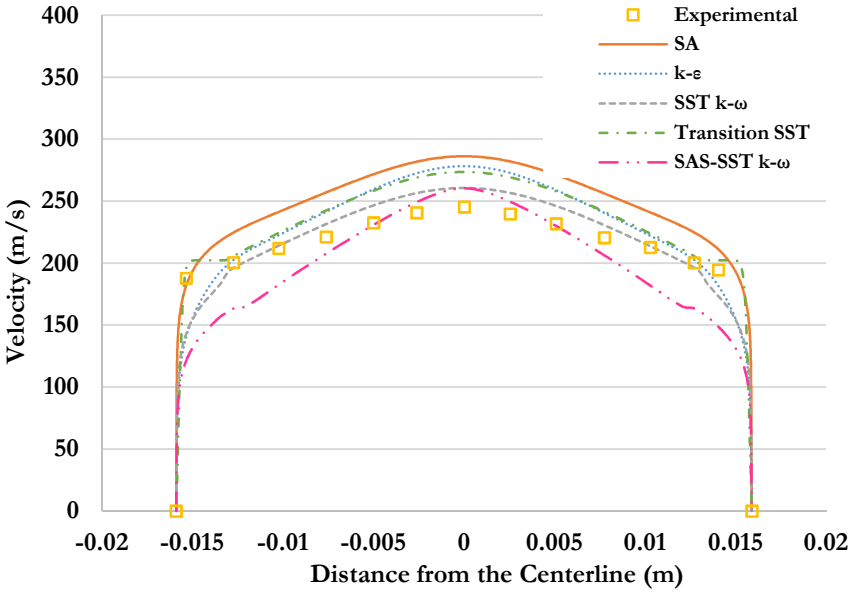

Figure 3.45 Run #5: Comparison of Velocity Profiles Computed using Various Turbulence Models with the Experimental Data at a Distance of 10.5 inches from the Nozzle Outlet.

The simulation results for the velocity profiles of runs #6, #7, #9, and #10 are shown in Figures 3.46-3.66. The computations show similar outcomes for each turbulence model when compared to the experiment as in the case of the 1.25" mixing section throat.

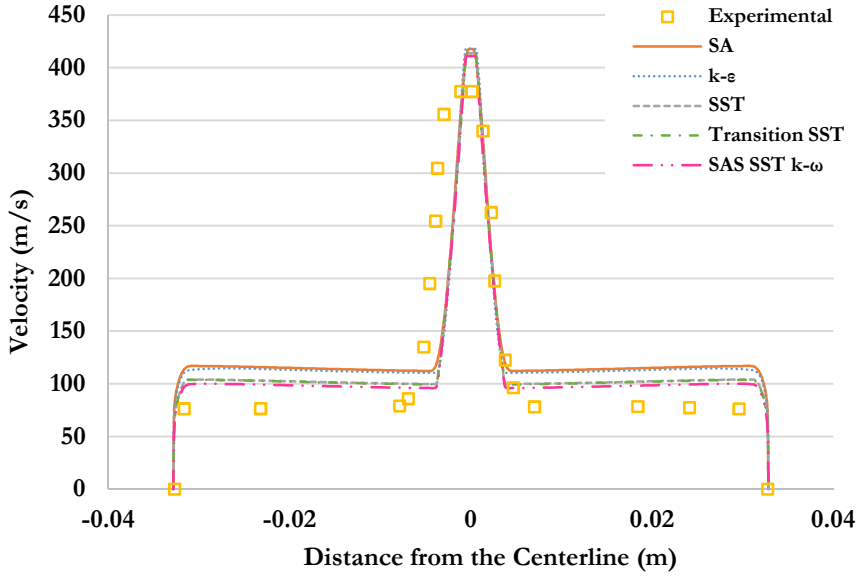

Figure 3.46 Run #6: Comparison of Velocity Profiles Computed using Various Turbulence Models with the Experimental Data at a Distance of 1 inch from the Nozzle Outlet.

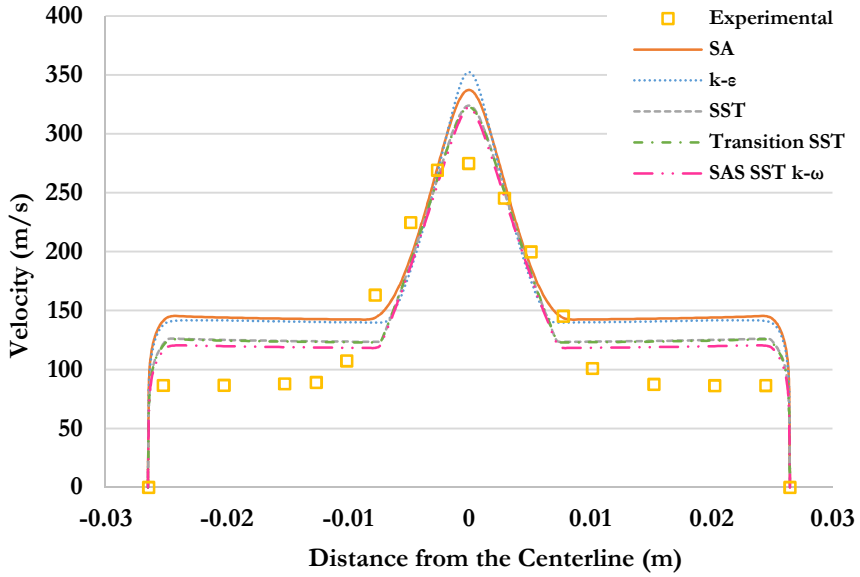

Figure 3.47 Run #6: Comparison of Velocity Profiles Computed using Various Turbulence Models with the Experimental Data at a Distance of 3 inches from the Nozzle Outlet.

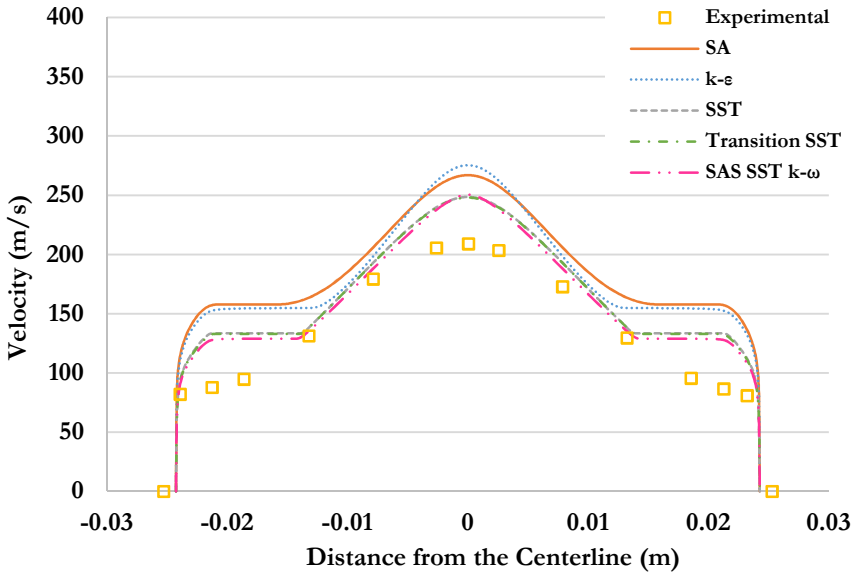

Figure 3.48 Run #6: Comparison of Velocity Profiles Computed using Various Turbulence Models with the Experimental Data at a Distance of 7 inches from the Nozzle Outlet.

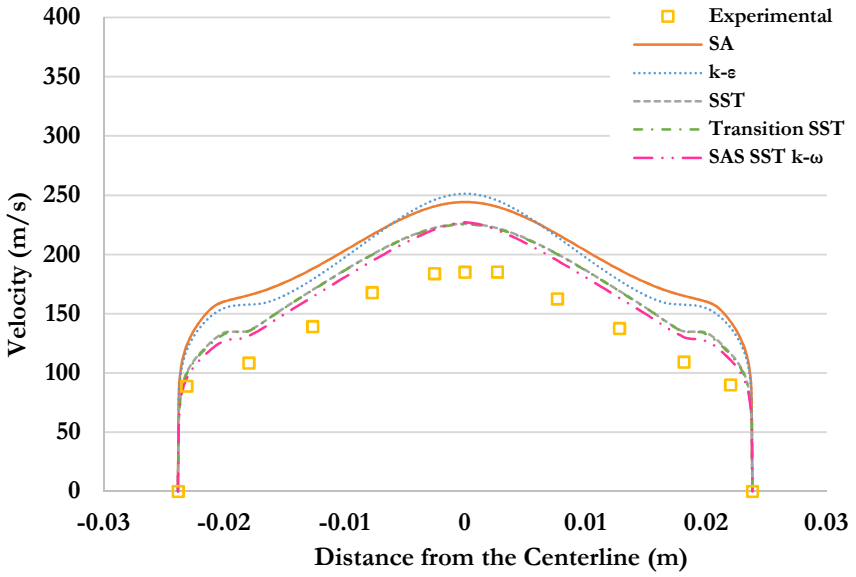

Figure 3.49 Run #6: Comparison of Velocity Profiles Computed using Various Turbulence Models with the Experimental Data at a Distance of 10.5 inches from the Nozzle Outlet.

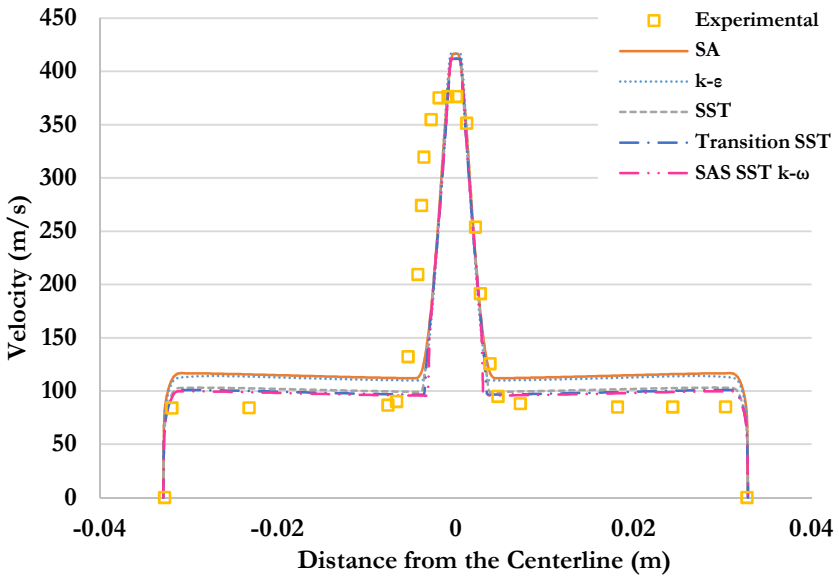

Figure 3.50 Run #7: Comparison of Velocity Profiles Computed using Various Turbulence Models with the Experimental Data at a Distance of 1 inch from the Nozzle Outlet.

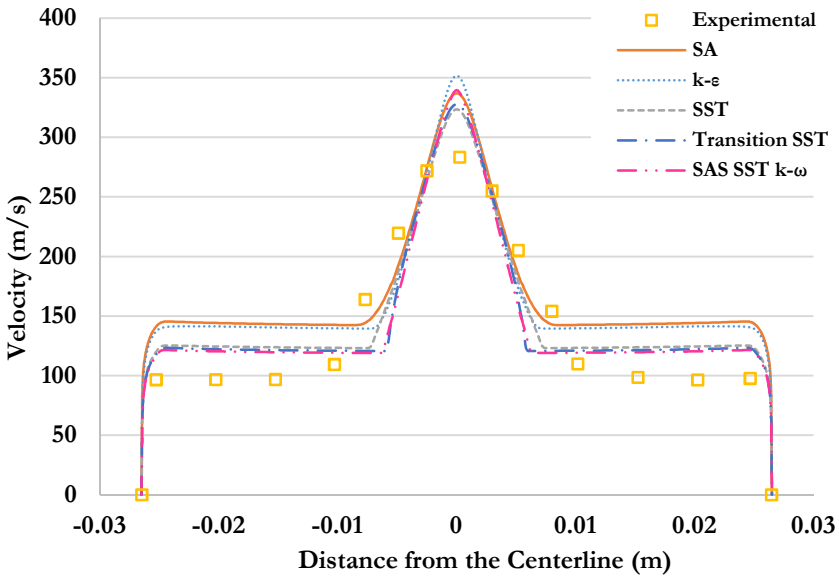

Figure 3.51 Run #7: Comparison of Velocity Profiles Computed using Various Turbulence Models with the Experimental Data at a Distance of 3 inches from the Nozzle Outlet.

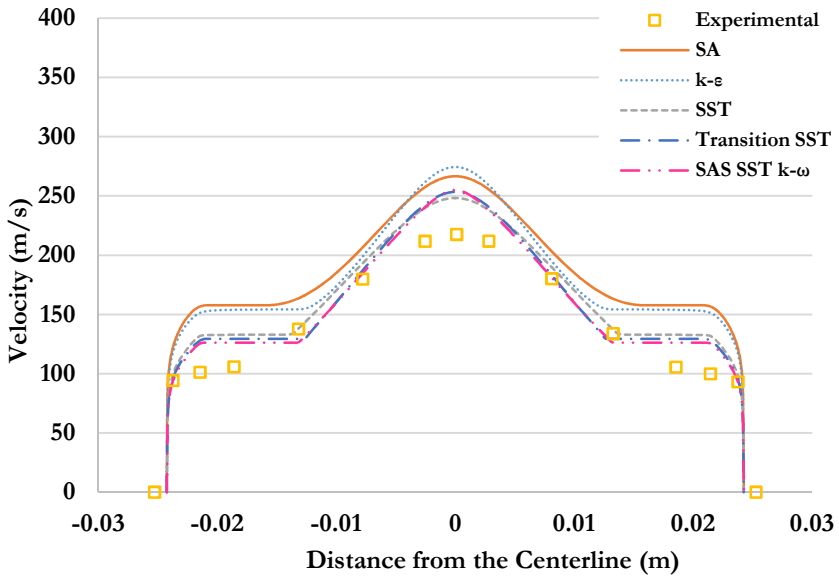

Figure 3.52 Run #7: Comparison of Velocity Profiles Computed using Various Turbulence Models with the Experimental Data at a Distance of 7 inches from the Nozzle Outlet.

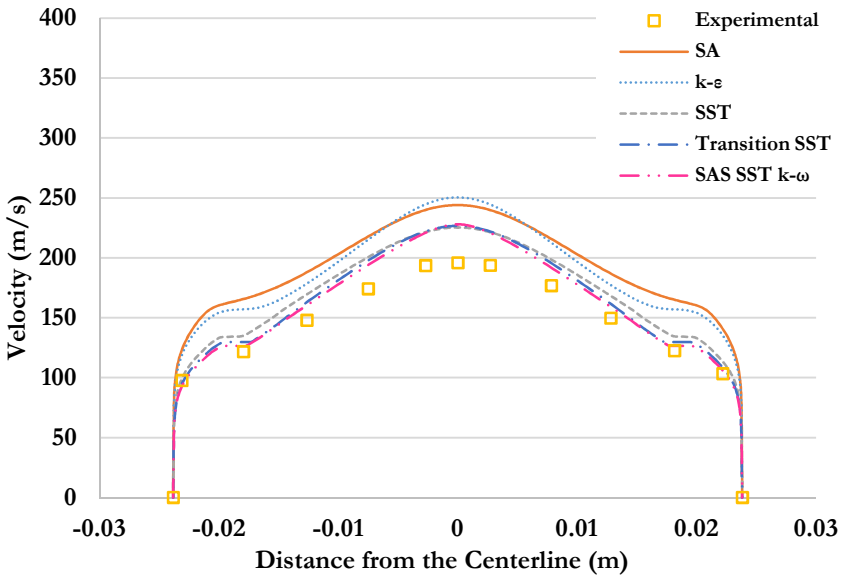

Figure 3.53 Run #7: Comparison of Velocity Profiles Computed using Various Turbulence Models with the Experimental Data at a Distance of 10.5 inches from the Nozzle Outlet.

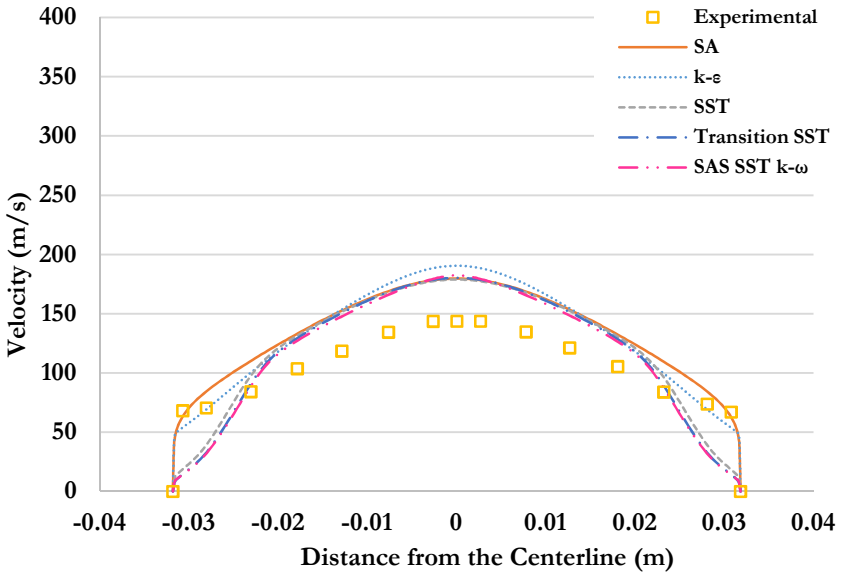

Figure 3.54 Run #7: Comparison of Velocity Profiles Computed using Various Turbulence Models with the Experimental Data at a Distance of 17 inches from the Nozzle Outlet.

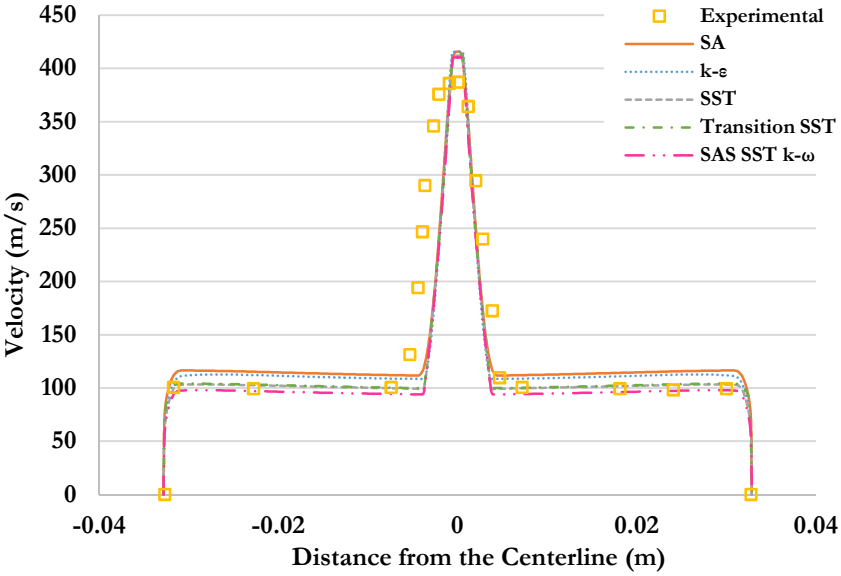

Figure 3.55 Run #9: Comparison of Velocity Profiles Computed using Various Turbulence Models with the Experimental Data at a Distance of 1 inch from the Nozzle Outlet.

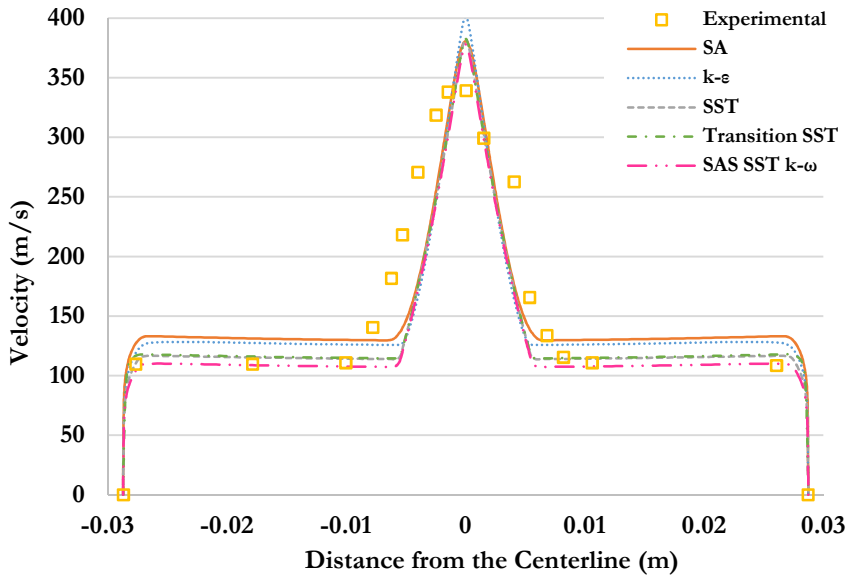

Figure 3.56 Run #9: Comparison of Velocity Profiles Computed using Various Turbulence Models with the Experimental Data at a Distance of 2 inches from the Nozzle Outlet.

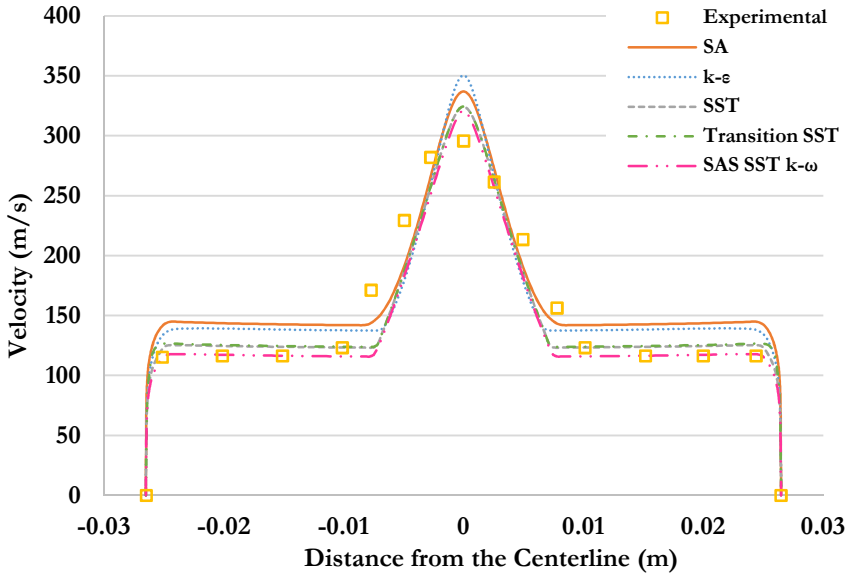

Figure 3.57 Run #9: Comparison of Velocity Profiles Computed using Various Turbulence Models with the Experimental Data at a Distance of 3 inches from the Nozzle Outlet.

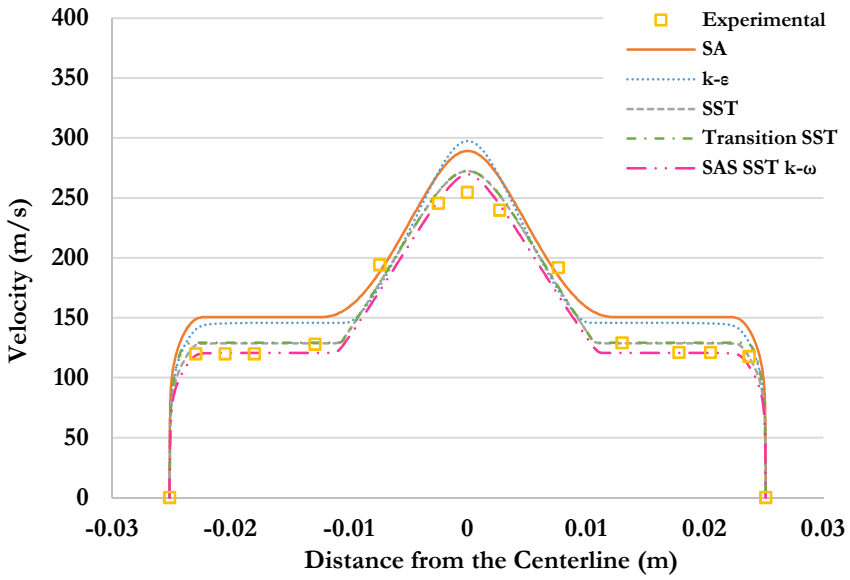

Figure 3.58 Run #9: Comparison of Velocity Profiles Computed using Various Turbulence Models with the Experimental Data at a Distance of 5 inches from the Nozzle Outlet.

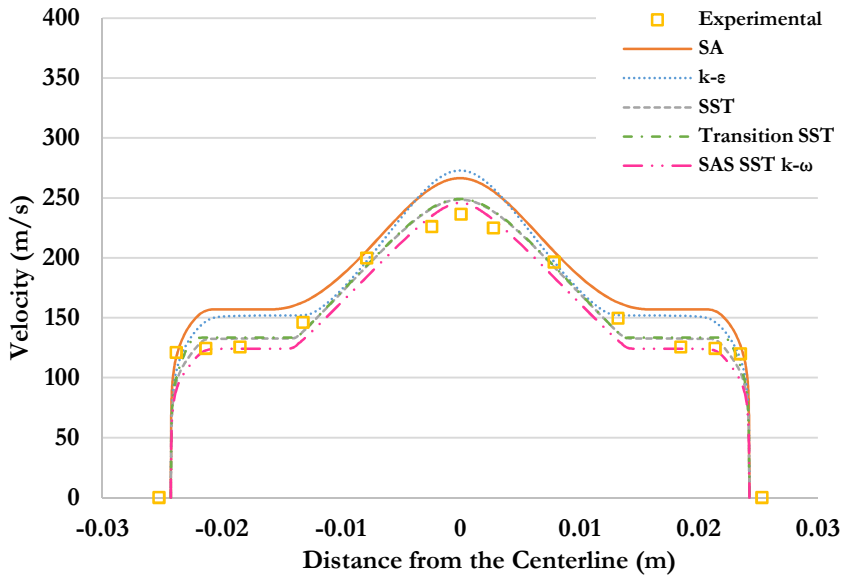

Figure 3.59 Run #9: Comparison of Velocity Profiles Computed using Various Turbulence Models with the Experimental Data at a Distance of 7 inches from the Nozzle Outlet.

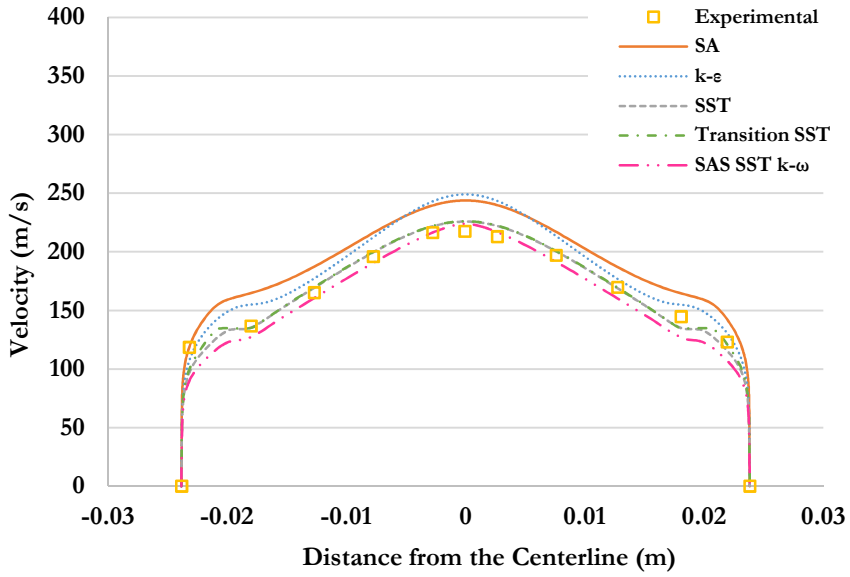

Figure 3.60 Run #9: Comparison of Velocity Profiles Computed using Various Turbulence Models with the Experimental Data at a Distance of 10.5 inches from the Nozzle Outlet.

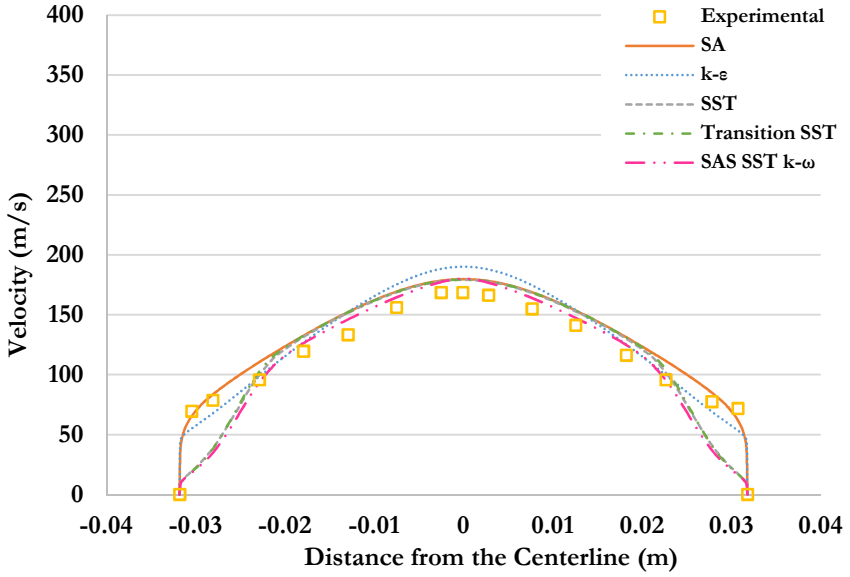

Figure 3.61 Run #9: Comparison of Velocity Profiles Computed using Various Turbulence Models with the Experimental Data at a Distance of 17 inches from the Nozzle Outlet.

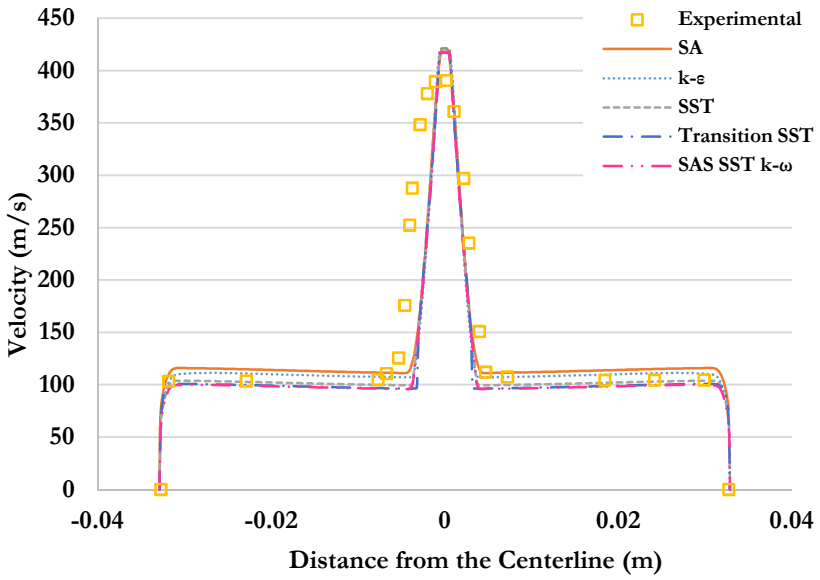

Figure 3.62 Run #10: Comparison of Velocity Profiles Computed using Various Turbulence Models with the Experimental Data at a Distance of 1 inch from the Nozzle Outlet.

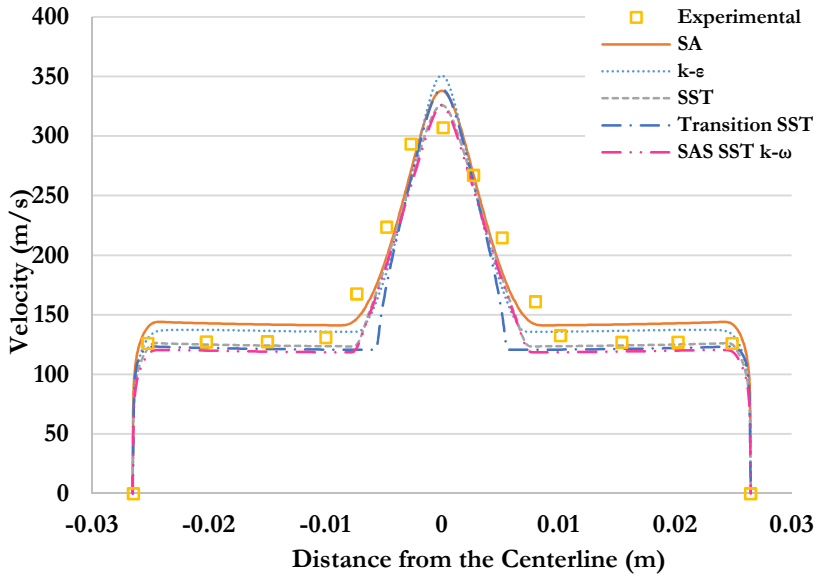

Figure 3.63 Run #10: Comparison of Velocity Profiles Computed using Various Turbulence Models with the Experimental Data at a Distance of 3 inches from the Nozzle Outlet.

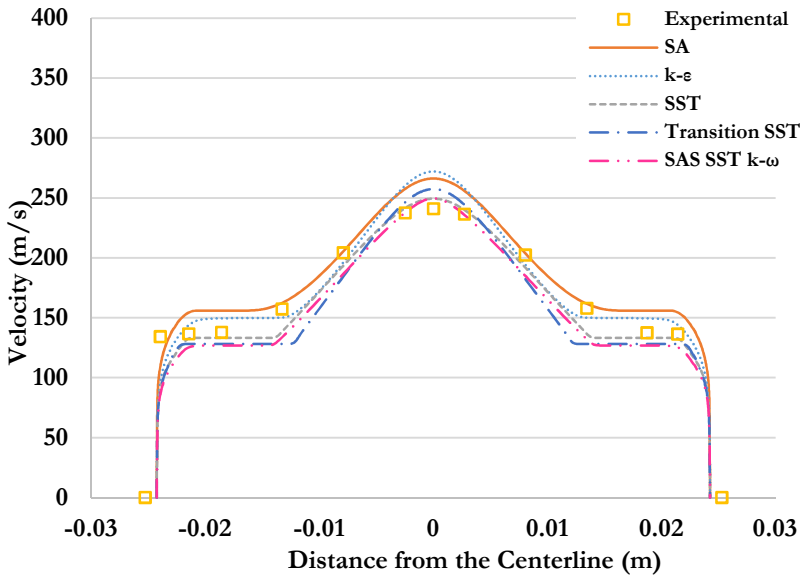

Figure 3.64 Run #10: Comparison of Velocity Profiles Computed using Various Turbulence Models with the Experimental Data at a Distance of 7 inches from the Nozzle Outlet.

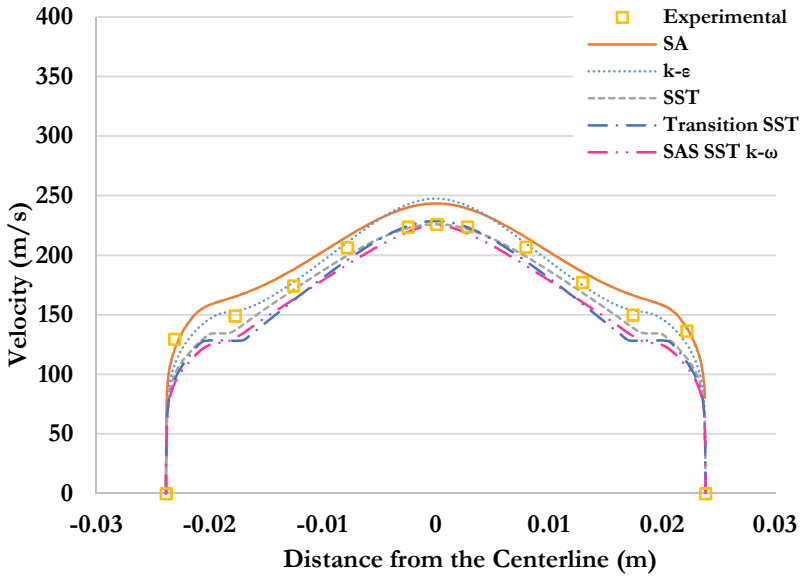

Figure 3.65 Run #10: Comparison of Velocity Profiles Computed using Various Turbulence Models with the Experimental Data at a Distance of 10.5 inches from the Nozzle Outlet.

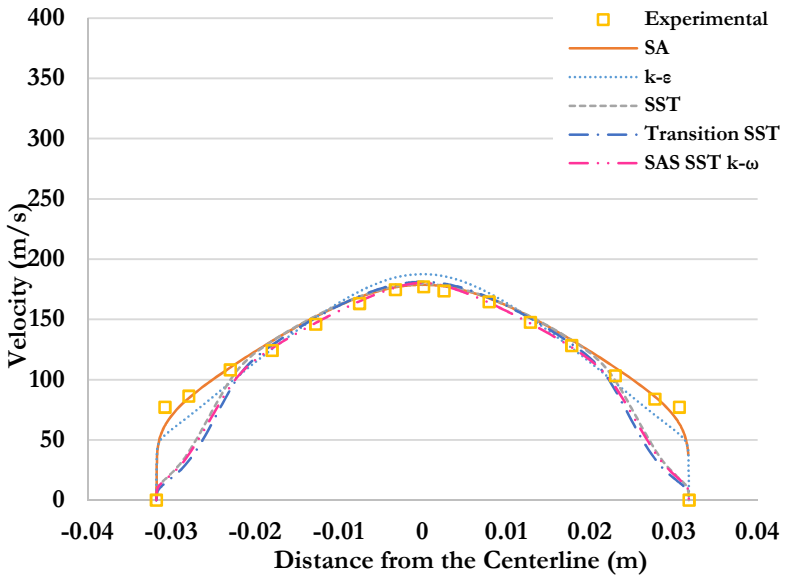

Figure 3.66 Run #10: Comparison of Velocity Profiles Computed using Various Turbulence Models with the Experimental Data at a Distance of 17 inches from the Nozzle Outlet.

The velocity profiles of run #5 and run #10 were calculated using the mass flow boundary condition at the nozzle inlet, these are plotted in Figures 3.67-3.74. For the first third of the mixing section, the SST *k-ω*, Transition SST, and SAS-SST *k-ω* models show the best agreement with the experimental data but as the flow becomes more uniform downstream, the SA and *k-ε* models produce better results.

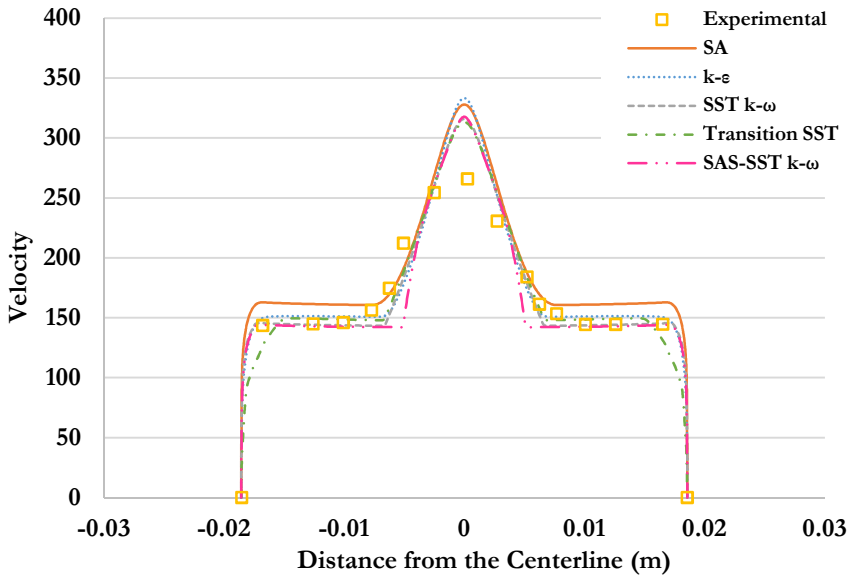

Figure 3.67 Run #5: Comparison of Velocity Profiles Computed using Various Turbulence Models with Mass Flow Rate Boundary Condition and the Experimental Data at a Distance of 3 inches from the Nozzle Outlet.

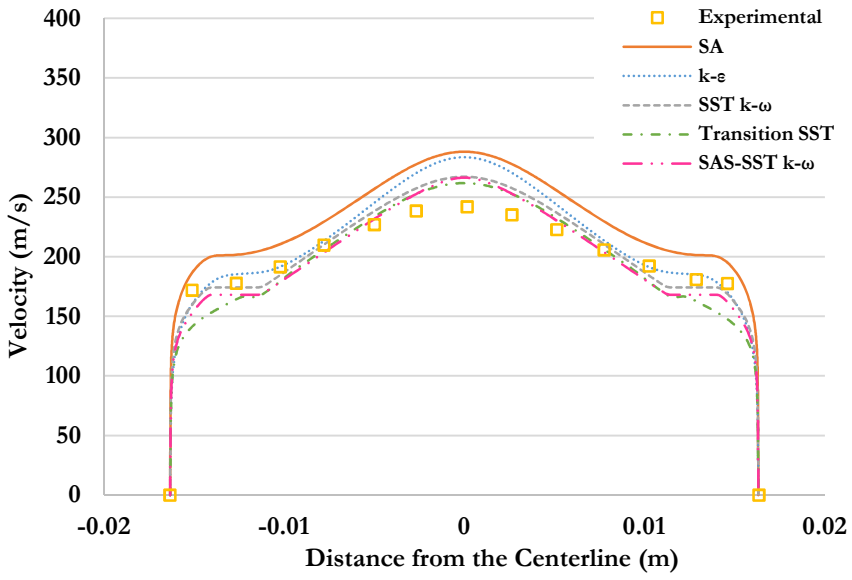

Figure 3.68: Run #5: Comparison of Velocity Profiles Computed using Various Turbulence Models with Mass Flow Rate Boundary Condition and the Experimental Data at a Distance of 7 inches from the Nozzle Outlet.

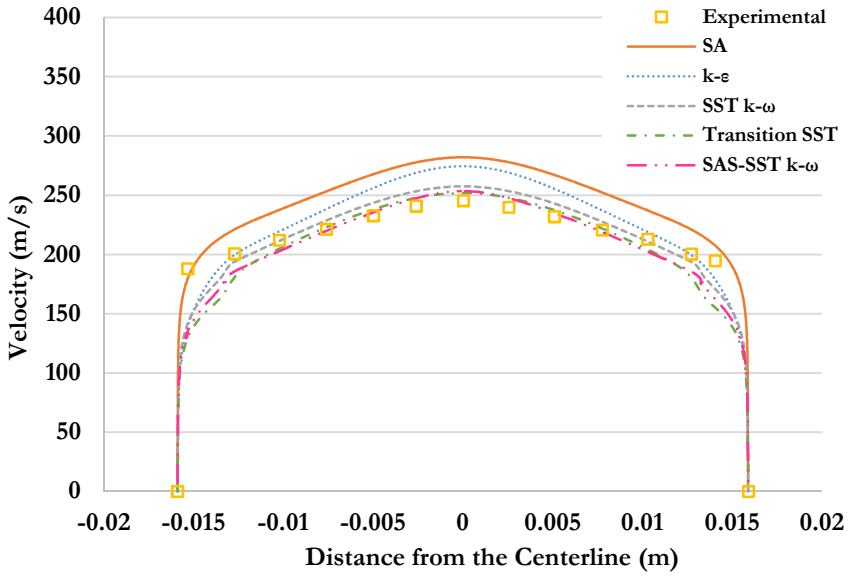

Figure 3.69: Run #5: Comparison of Velocity Profiles Computed using Various Turbulence Models with Mass Flow Rate Boundary Condition and the Experimental Data at a Distance of 10.5 inches from the Nozzle Outlet.

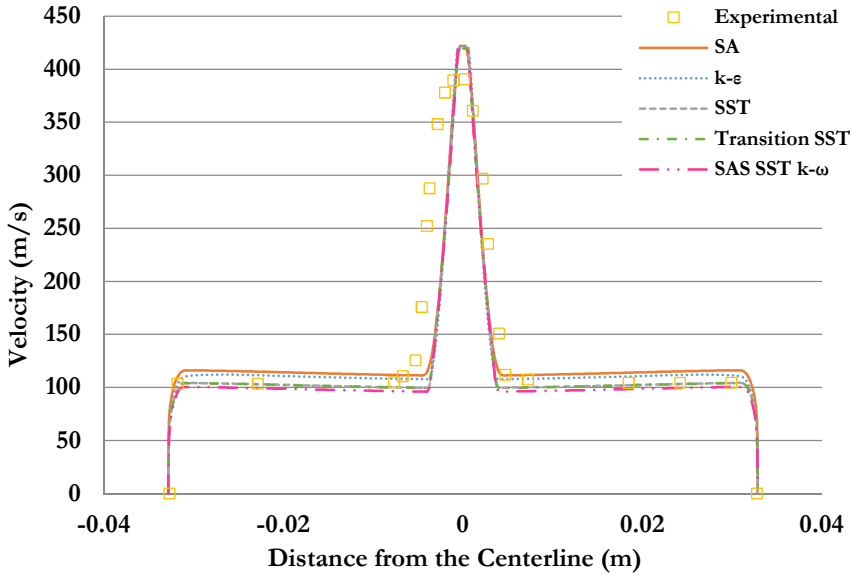

Figure 3.70: Run #10: Comparison of Velocity Profiles Computed using Various Turbulence Models with Mass Flow Rate Boundary Condition and the Experimental Data at a Distance of 1 inch from the Nozzle Outlet.

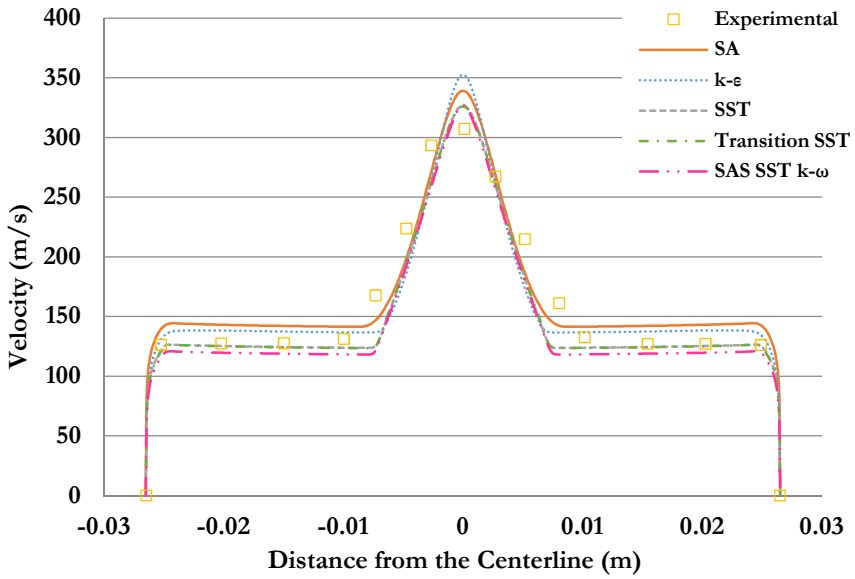

Figure 3.71: Run #10: Comparison of Velocity Profiles Computed using Various Turbulence Models with Mass Flow Rate Boundary Condition and the Experimental Data at a Distance of 3 inches from the Nozzle Outlet.

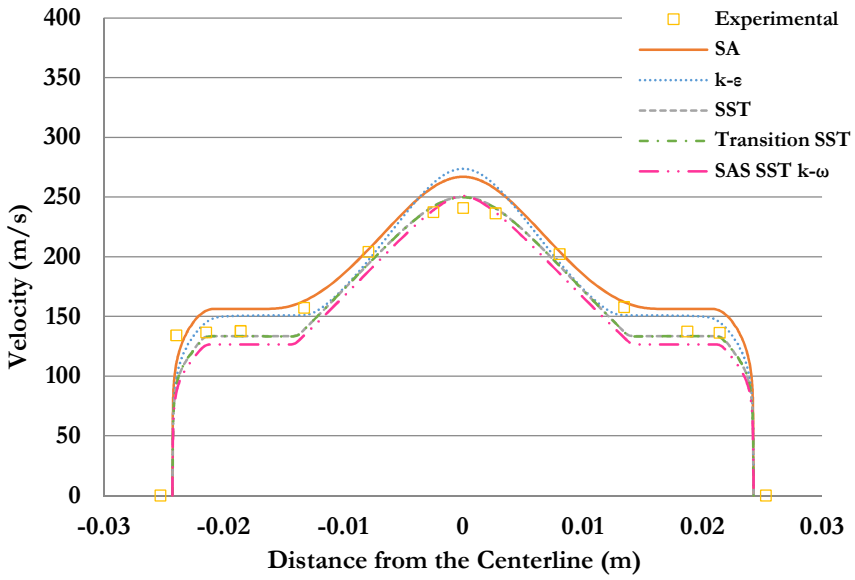

Figure 3.72: Run #10: Comparison of Velocity Profiles Computed using Various Turbulence Models with Mass Flow Rate Boundary Condition and the Experimental Data at a Distance of 7 inches from the Nozzle Outlet.

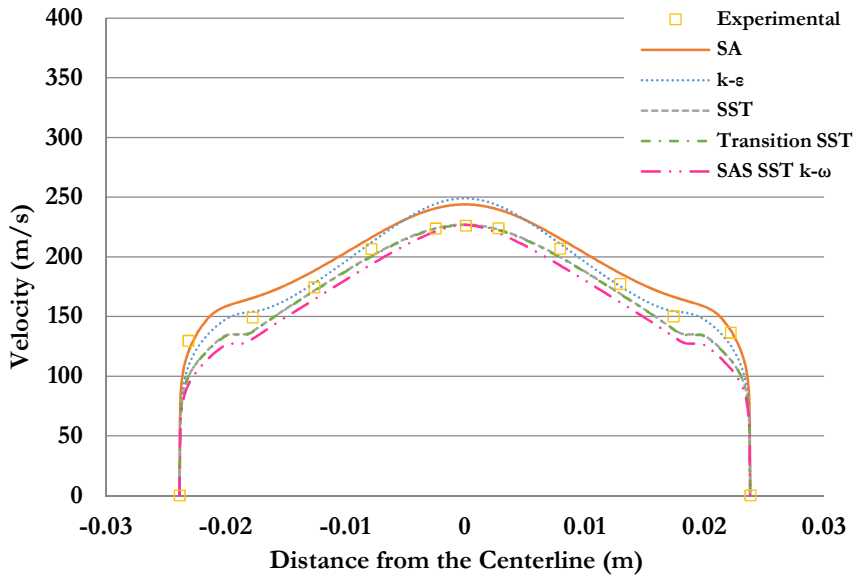

Figure 3.73: Run #10: Comparison of Velocity Profiles Computed using Various Turbulence Models with Mass Flow Rate Boundary Condition and the Experimental Data at a Distance of 10.5 inches from the Nozzle Outlet.

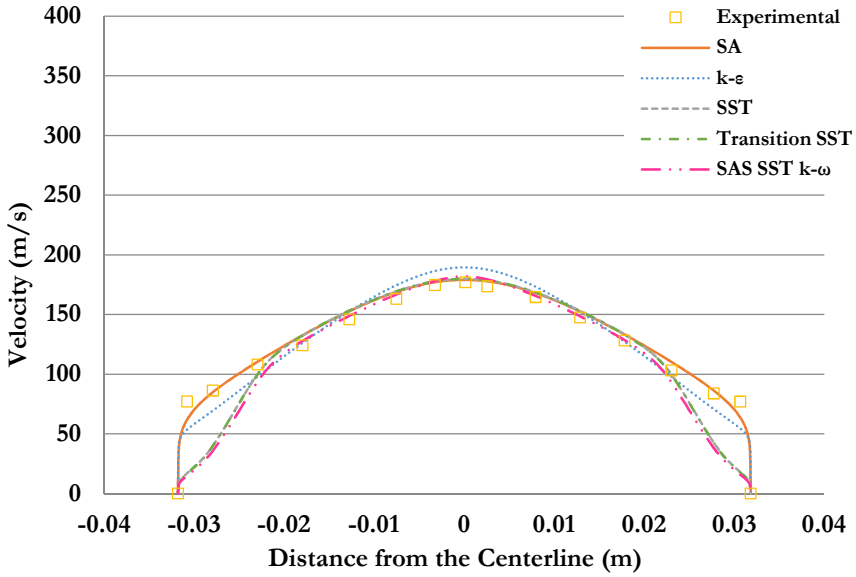

Figure 3.74: Run #10: Comparison of Velocity Profiles Computed using Various Turbulence Models with Mass Flow Rate Boundary Condition and the Experimental Data at a Distance of 17 inches from the Nozzle Outlet.

4 Conclusions and Future Research

4.1 Conclusions

In the past several decades, CFD modeling has become an essential part in the analysis and design of various industrial products. In this thesis, by comparing the results of CFD simulations using five different turbulence models with the experimental data, we were able to determine the best turbulence model for accurately simulating the flow field of a 2D slot nozzle ejector. As the results in the thesis show, the SST *k-ω* and Transition SST *k-ω* turbulence models produce the best comparisons with the experimental data. The Transition SST *k-ω* turbulence model produced the most accurate mass flow rates and the ratios between the nozzle mass flow and the entrained flow in the mixing section for all experimental test runs. The SST *k-ω* model produced the best results for the velocity profiles at various sections of the nozzle-ejector configuration. Both the SST *k-ω* and Transition SST *k-ω* models produced the best results for the centerline velocity profiles along the nozzle-ejector axis. The Transition SST *k-ω* model with 2nd and 3rd order accurate numerical simulation gave good results but resulted in some oscillations in mass flow rate. Greater oscillations occurred when 3rd order accurate scheme was employed. The SAS-SST *k-ω* model resulted in a close match with the experimental data but also produced some small oscillations in the converged solution. Also, this model was computationally most expensive and required the longest time to converge. The SA and k-ε turbulence models produced the least accurate results among all the models. In conclusion, overall the SST k-ω model performed the best in terms of accuracy, stability and efficiency of the computed solutions.

4.2 Future Research

The future work in this field of research can take place in several directions. A complete 3D model could be simulated which would allow for the inclusion of the plenum, orifice, and the throttle valve downstream of the mixing section. More complex physical models such as the Detached Eddy Simulation (DES) and Large Eddy Simulation (LES) can be employed for better resolution of the details of the flow field. The optimization of the shape of the slot nozzle ejector can also be useful for optimizing its efficiency.

References

[1] G. B. Gilbert and P. G. Hill, "Analysis and Testing of Two-Dimensional Slot Nozzle Ejectors with Variable Area Mixing Sections," NASA CR-2251, 1973.

[2] J. C. Tannehill, D. A. Anderson, and R. H. Pletcher, *Computational Fluid Mechanics and Heat Transfer*, Second Edition, Hemisphere, New York, 1997

[3] N. J. Georgiadis and D. A. Yoder, "Use of Navier-Stokes Methods for the Calculation of High-Speed Nozzle Flow Fields," AIAA paper 94-3212, 30th AIAA Joint Propulsion Conference, Indianapolis, IN, USA, June 1994.

[4] ANSYS FLUENT 14.5, Theory Guide, ANSYS Inc., Canonsburg, PA, USA, 2012.

[5] S. B. Pope, *Turbulent Flows*, Cambridge University Press, 2000.

[6] F. R.Menter, "Zonal Two Equation k-ω Turbulence Model for Aerodynamic Flows," AIAA paper 93-2906, 24th AIAA Fluid Dynamics Conference, Orlando, FL, USA, July 1993.

Vita

Colin T. Graham

Degrees	M.S. Mechanical Engineering, August 2014 B.S. Mechanical Engineering, December 2008
Professional Societies	American Institute of Aeronautics and Astronautics
Publications	Ryan, Clegg, Gabrielle Coutrot, John Fetrow, Michael Gidding, Colin Graham, Adam Mendelsohn, Sarah Valencia, Michael Yue, Michael Zanetti, and Ramesh Agarwal. "Polar Exploration and Reconnaissance for Lunar Studies," *Frontiers in Aerospace Engineering*, Vol. 2, No. 4, 2013.